Engineering Analysis with Boundary Elements 179 (2025) 106367

Contents lists available at ScienceDirect

Engineering Analysis with Boundary Elements

journal homepage: www.elsevier.com/locate/enganabound

Adaptive RBF-FD meshless solution of 3D fluid flow and heat transfer problems

Luca Bacer [a],*, Riccardo Zamolo [a], Davide Miotti [b], Enrico Nobile [a]

[a] Department of Engineering & Architecture, Università degli Studi di Trieste, via Alfonso Valerio 10, Trieste, 34127, Italy
[b] Scuola Internazionale Superiore di Studi Avanzati (SISSA), via Bonomea 265, Trieste, 34136, Italy

ARTICLE INFO

MSC:
80M22

Keywords:
Meshless
Radial Basis Function-Finite Differences (RBF-FD)
Navier–Stokes
Adaptivity
Error indicator

ABSTRACT

This paper describes an adaptive approach for the solution of 3D steady and incompressible flows with the RBF-FD (Radial Basis Function-Finite Difference) meshless method. This method relies on a set of scattered nodes in the domain instead of a traditional mesh data structure. The lack of connectivity information and the absence of the mesh generation make the RBF-FD method particularly advantageous for the accurate numerical solution of many problems of engineering interest. Furthermore, automatic node generation is possible thanks to many algorithms that recently have been proposed. However, as it happens for mesh-based methods, the accurate solution of partial differential equations usually require proper node distributions with higher node density in specific areas. The approach described in this paper allows the re-generation of the entire node distribution in order to minimize some error indicator by automatically adjusting local node density depending on the domain and physical problem. The main contribution of this work is the introduction of some original error indicators which are used for the aforementioned adaptive node generation and the assessment of their effect on accuracy. Results show good convergence properties and highlight some differences in the behavior of the different adaptive approaches in the spatial error distribution.

1. Introduction

Thanks to the rapid growth of computational resources and the capability to easily manipulate huge amount of data, the use of CAE (Computer Aided Engineering) software is becoming pervasive in almost all areas of engineering. CAE software often makes use of numerical methods to simulate a very wide range of phenomena of practical industrial relevance. With particular reference to CFD (Computational Fluid Dynamics), where the goal is to numerically solve PDEs (Partial Differential Equations) that are used to model fluid flow and heat transfer problems, up to now most commercial and open source solvers rely on mesh-based methods such as FEM (Finite Element Method) of FVM (Finite Volume Method). The mesh generation phase required by mesh-based methods can be very expensive and time consuming, as a high quality mesh is needed to obtain accurate result, which in turn often requires a specialized human operator. In order to avoid the need of a mesh altogether, different meshless methods have been developed [1,2]. Such methods typically require only a set of scattered nodes in the domain, while connectivity information between the nodes is no longer needed, allowing greater geometrical flexibility.

In the last years several node generation techniques for meshless methods have been proposed: advancing-front methods [3,4], refinement-based algorithms [3,5], Poisson disk sampling [6,7]. However, like in mesh-based methods, using a uniform node distribution leads to unnecessary high node density where it is not needed and, at the same time, low node density where the solution exhibits large spatial variations, e.g., boundary layers or interfaces. In order to optimally solve this problem, adaptive strategies that iteratively update the discretization based on the solution itself can be employed, where the ultimate goal is to obtain a uniform error over the whole domain. Adaptive approaches for CFD problems have been widely studied over the years and are well established in mesh-based solvers [8–12]. However, adaptive techniques for newly proposed meshless methods are investigated in a very limited way to date. In 2009, Angulo et al. [13] proposed one of the first adaptive approaches in the context of meshless methods, followed by other approaches [14–19]. This paper aims to fill this gap in the bibliography by proposing different adaptive strategies that are suitable to be used in the context of fluid flow and heat transfer problems solved by the RBF-FD (Radial Basis Function-Finite Difference) method [20–22].

Adaptive approaches are mainly of three types: *h*-refinement, where cells or nodes are added in the mesh or node distribution, *p*-refinement, where the order of accuracy of the adopted numerical scheme is

* Corresponding author.
E-mail addresses: luca.bacer@phd.units.it (L. Bacer), rzamolo@units.it (R. Zamolo), nobile@units.it (E. Nobile).

https://doi.org/10.1016/j.enganabound.2025.106367
Received 28 January 2025; Received in revised form 20 June 2025; Accepted 22 June 2025
Available online 8 July 2025

Nomenclature

N	Total number of nodes
N_B	Number of boundary nodes
N_I	Number of internal nodes
m	Number of nodes in the stencil
m_I	Number of internal nodes in the stencil
q	Size of polynomial basis
P	Polynomial degree
S	Stencil
Nu	Nusselt number
Nu_θ	Relative error of local Nusselt number
C_d	Drag coefficient
Pr	Prandtl number (ν/α)
Ra	Rayleigh number
Re	Reynolds number ($u_0 d_H/\nu$)
$\hat{e}$	Error indicator
$\tilde{e}$	Smoothed error indicator
x, y, z	Coordinates
s	Spacing function
p	Pressure
T	Temperature
t	Time
Δt	Timestep
g	Gravitational acceleration
$\boldsymbol{u}$	Velocity vector (u_x, u_y, u_z)
$\boldsymbol{u}^h$	Approximated velocity
$\boldsymbol{u}^*$	Tentative velocity
u_0	Reference velocity
$\boldsymbol{z}$	Unit vector along vertical axis

Greek symbols

α	Thermal diffusivity
β	Volumetric thermal expansion
γ	Nodal growth rate
ε	Shape factor
κ	Thermal conductivity
ν	Kinematic viscosity
Ω	Domain
ρ	Density
ρ_0	Reference density
τ	Value for the adaptive approach
θ	Polar angle
ϕ	Auxiliary correction variable

Superscripts and Symbols

^{k}	Quantity relative to the kth adaptive iteration
^{l}	Time level

increased, and r-refinement, where the mesh [12] or node distribution is moved maintaining its topology. In this paper we focused on the h-refinement by generating a completely new node distribution for each adaptive iteration. Different error indicators can be used to drive both mesh-based and meshless adaptivity [23]. Most error indicators can be divided into two categories: recovery-based error indicators, which rely on the reconstruction of solution gradients or solution curvature, and residual-based error indicators, which aim to estimate truncation errors. Even if the majority of meshless and mesh-based adaptive approaches are based on the first category, error indicators based on the second category have a stronger theoretical foundation [23]. The main novelty introduced in this work is the use of two original residual-based error indicators that are suitable for the RBF-FD meshless solution of 3D fluid flow problems, with particular reference to steady-state, laminar and incompressible flows, both isothermal and non-isothermal, i.e., with heat transfer. The first error indicator is based on the estimation of the residual arising from the spatial discretization of the momentum or energy equation; the second one is based on the estimation of the residual of the continuity equation. To the best of the authors' knowledge, this is the first time that such error indicators are applied and compared in this context. We also compare the results with a recovery-based error indicator developed for the same RBF-FD meshless approach [7,19].

The resulting adaptive approaches have been applied to four different 3D fluid flow problems: a natural convection problem in a spherical shell, a forced convection problem in a pipe with a spherical obstacle, an isothermal fluid flow problem within the same pipe and a fully developed isothermal fluid flow problem in a triply periodic minimal surface (TPMS) structure employed in compact heat exchangers [24]. Comparisons are carried out quantitatively in terms of nondimensional integral quantities, i.e., Nusselt number for non-isothermal cases and drag coefficient and Fanning friction factor for the isothermal cases, and also qualitatively in terms of error uniformity over the domain.

The paper is organized as follows: in Section 2 the governing equations for the considered problems are described. In Section 3 the RBF-FD meshless method is briefly described and the proposed adaptive approach is presented together with the employed error indicators. In Section 4 the considered fluid flow problems are thoroughly described and in Section 5 the results for the considered problems are presented and discussed.

2. Problem definition

Laminar, incompressible and steady-state 3D problems are considered. In addition, three of four problems are axisymmetric, which allow for very accurate reference results. However, in order to assess the applicability and performance of the adaptive meshless approaches, a 3D formulation is considered also for the axisymmetric problems, which is more relevant for industrial applications.

2.1. Governing equations

The considered fluid flow problems with possible heat transfer are described by the following dimensionless conservation equations of mass, momentum and energy:

$$\nabla \cdot \boldsymbol{u} = 0, \tag{1}$$

$$\frac{\partial \boldsymbol{u}}{\partial t} + (\boldsymbol{u} \cdot \nabla)\boldsymbol{u} = -\nabla p + \frac{1}{A}\nabla^2 \boldsymbol{u} + B\boldsymbol{z}, \tag{2}$$

$$\frac{\partial T}{\partial t} + \boldsymbol{u} \cdot \nabla T = \frac{1}{C}\nabla^2 T, \tag{3}$$

where $\boldsymbol{u} = (u, v, w)$ is the velocity, t the time, T the temperature, p the pressure, $\boldsymbol{z}$ the unit vector along the vertical axis and A, B, C are coefficients that depend on each problem (see Section 4). Although all the considered problems are steady-state, the time dependent formulation is here considered because of the solution procedure presented in Section 3.1.3. For the periodic flow in the TPMS structure, the pressure is decomposed into periodic $\tilde{p}$ and linear components as follows:

$$p = \tilde{p} - \beta x \tag{4}$$

where β is a fixed pressure gradient along the streamwise direction x. More details on the mathematical formulation for this case can be found in [24].

3. Numerical method

In this section a brief description of the employed numerical method is given. This section is divided into two main subsections: one regarding the RBF-FD method and the solution procedure, and one concerning the adaptive approach.

3.1. RBF-FD method and solution procedure

3.1.1. Meshless node generation

The node distributions required by the RBF-FD meshless method are obtained by using the node repel refinement algorithm developed by Zamolo and Nobile [5] and is briefly presented as follows.

Given the domain Ω and its boundary $\partial\Omega$, the node generation process can be divided in two phases:

- generation of an initial node distribution in Ω that satisfies a certain spacing function $s(\boldsymbol{x})$ on average. The spacing function defines the average (variable) distance between a point and its neighboring nodes. This initial node distribution does not conform to the boundaries.
- iterative refinement on the initial node distribution with a node-repel approach [3]. The nodes are iteratively moved according to mutual repulsion forces defined as a function of spacing $s(\boldsymbol{x})$ and distance between any two nodes. The process is iterated until a sought node distribution is reached. During this phase, when a node is pushed outside the domain Ω, it is projected on the nearest point on the boundary, resulting in a boundary conforming node distribution.

3.1.2. RBF-FD method

The employed RBF-FD method is based on the Hermite interpolation with a polynomial augmentation [25–27]. The goal is to find a suitable function u^h that interpolates nodal values using a RBF expansion. The considered Hermite RBF expansion is the following:

$$u^h(\boldsymbol{x}) = \sum_{i=1}^{m_I} \alpha_i \varphi_i(\boldsymbol{x}) + \sum_{i=m_I+1}^{m} \alpha_i \mathcal{B}\varphi_i(\boldsymbol{x}) + \sum_{j=1}^{q} \beta_j p_j(\boldsymbol{x}) \tag{5}$$

where $\varphi_i(\boldsymbol{x}) = \varphi(\|x - x_i\|)$ are the RBFs centered at the m stencil nodes $\boldsymbol{x}_i$, m_I is the number of internal nodes of the stencil. The second term refers to the boundary conditions and $\{p_j\}_{j=1}^{q}$ is a polynomial basis of the multivariate polynomial space Π_P^d of total degree P in d dimensions. $\mathcal{B}$ is the linear operator associated to the boundary conditions, expressed by $\mathcal{B}u = g$. For this paper we have employed the MultiQuadric RBF (MQ) [22,28–30]:

$$\varphi(r) = \sqrt{1 + (\varepsilon r)^2} \tag{6}$$

where $r = \|\boldsymbol{x} - \boldsymbol{x}_i\|$, with $\{\boldsymbol{x}_i\}_{i=1}^{m}$ the interpolation stencil of size m. In this paper the number of nodes m considered in each stencil is fixed such that $m = 2q$, with q the size of the polynomial basis. Such a strategy is common and is known to be a good choice in terms of accuracy and stability [31–33] (the reader is referred to [34] for more recent observations regarding the dependence of RBF-FD accuracy on stencil size). The shape parameter is chosen such that $\varepsilon = 0.4/s(\boldsymbol{x})$.

In order to find the weights values $\{\alpha_1, \dots, \alpha_m\}$ and $\{\beta_1, \dots, \beta_q\}$, interpolation conditions are imposed:

$$u^h(\boldsymbol{x}_i) = u(\boldsymbol{x}_i), \;\; i = 1, \dots, m_I \tag{7}$$

If the stencil includes some boundary nodes, the boundary conditions are imposed:

$$\mathcal{B}u^h(\boldsymbol{x}_i) = g(\boldsymbol{x}_i), \;\; \boldsymbol{x}_i \in \partial\Omega \tag{8}$$

Additional orthogonality conditions are then enforced in order to ensure a unique solution [35].

By writing the above equations in a more compact shape, the following symmetric linear system is obtained:

$$\underbrace{\begin{bmatrix} \boldsymbol{\varphi}_{\mathrm{BC}} & \boldsymbol{P} \\ \boldsymbol{P}^T & 0 \end{bmatrix}}_{\boldsymbol{M}} \begin{pmatrix} \boldsymbol{\alpha} \\ \boldsymbol{\beta} \end{pmatrix} = \begin{pmatrix} \boldsymbol{u} \\ \boldsymbol{g} \\ \boldsymbol{0} \end{pmatrix} \tag{9}$$

where $(\boldsymbol{\alpha}\ \boldsymbol{\beta}) = \{\alpha_1, \dots, \alpha_m, \beta_1, \dots, \beta_q\}$ is the vector of the expansion coefficients and matrices $\boldsymbol{\varphi}_{\mathrm{BC}}$, $\boldsymbol{P}$, $\boldsymbol{u}$ and $\boldsymbol{g}$ are derived from Eqs. (7) and (8).

Given a linear PDE $\mathcal{L}u = f$, with $\mathcal{L}$ linear differential operator, u unknown function and f the known term, the operator $\mathcal{L}$ is applied to (5) in order to obtain

$$\begin{aligned} \mathcal{L}u^h(\boldsymbol{x}) &= \sum_{i=1}^{m_i} \alpha_i \mathcal{L}\varphi_i(\boldsymbol{x}) + \sum_{i=m_I+1}^{m} \alpha_i \mathcal{L}\mathcal{B}\varphi_i(\boldsymbol{x}) + \sum_{j=1}^{q} \beta_j \mathcal{L}p_j(\boldsymbol{x}) \\ &= \begin{pmatrix} \boldsymbol{\alpha} & \boldsymbol{\beta} \end{pmatrix} \begin{pmatrix} \Psi(\boldsymbol{x}) \\ \Pi(\boldsymbol{x}) \end{pmatrix} \end{aligned} \tag{10}$$

where $\Psi(\boldsymbol{x}) = \{\mathcal{L}\varphi_1(\boldsymbol{x}) \dots \mathcal{L}\varphi_m(\boldsymbol{x})\}$ and $\Pi(\boldsymbol{x}) = \{\mathcal{L}p_1(\boldsymbol{x}) \dots \mathcal{L}p_q(\boldsymbol{x})\}$.

By solving Eq. (9) for the expansion coefficients we obtain:

$$\begin{pmatrix} \boldsymbol{\alpha} \\ \boldsymbol{\beta} \end{pmatrix} = \boldsymbol{M}^{-1} \begin{pmatrix} \boldsymbol{u} \\ \boldsymbol{g} \\ \boldsymbol{0} \end{pmatrix} \tag{11}$$

which can be used in Eq. (10) to obtain the finite difference formula

$$\mathcal{L}u^h(\boldsymbol{x}) = \boldsymbol{c}^T \begin{pmatrix} \boldsymbol{u} & \boldsymbol{g} & \boldsymbol{0} \end{pmatrix} \tag{12}$$

$\boldsymbol{c}$ is the vector of finite difference coefficients that can be computed by solving the following linear system:

$$\boldsymbol{M}^T \boldsymbol{c} = \begin{pmatrix} \Psi(\boldsymbol{x}) \\ \Pi(\boldsymbol{x}) \end{pmatrix} \tag{13}$$

The FD formula (12) is made valid for each internal node $\boldsymbol{x}_i$ and, by using the corresponding finite difference coefficients, the following sparse linear system is obtained:

$$\boldsymbol{C}\boldsymbol{u}^h = \boldsymbol{q} - \boldsymbol{f} \tag{14}$$

where $\boldsymbol{u}^h = \{u^h(\boldsymbol{x}_1), \dots, u^h(\boldsymbol{x}_{N_I})\}$ is the vector of the unknown scalar values $u^h(\boldsymbol{x}_i)$ evaluated at the N_I internal nodes, $\boldsymbol{q}$ derives from the known terms of the FD formula (12), $\boldsymbol{C}$ is the sparse matrix built from the local finite difference coefficients and $\boldsymbol{f}$ is the vector obtained from the known term of the PDE, i.e., $f_i = f(x_i)$. The vector $\boldsymbol{u}^h$ represents the approximated solution of the considered PDE. We remark that the employed approach differs from the Hermitian method described by Stevens et al. [36] where PDE governing and boundary operators are directly applied to the RBFs within the solution construction [36]. In the approach used here, only the boundary operators are applied to the RBFs, while the collocation of PDEs is performed later by assembling the resulting discrete operators for the fundamental operators, i.e., gradient and Laplacian.

The reader is referred to [33,37,38] for more details on the stability of the RBF-FD method.

3.1.3. Solution procedure

The spatial derivatives composing PDEs (1), (2) and (3), are discretized in space by using the RBF-FD method. A projection scheme [39, 40] with a three-level backward Euler (or Gear) scheme is used for the time discretization.

A tentative velocity $\boldsymbol{u}^*$ is obtained from the linearized and discretized momentum equation (2):

$$\frac{3\boldsymbol{u}^* - 4\boldsymbol{u}^l + \boldsymbol{u}^{l-1}}{2\Delta t} + \boldsymbol{u}^l \nabla \boldsymbol{u}^* = -\nabla p^l + \frac{1}{A}\nabla^2 \boldsymbol{u}^* + B^l \boldsymbol{z} \tag{15}$$

where l is the time level and Δt is the timestep. Then $\boldsymbol{u}^*$ is forced to satisfy the continuity equation (1) by means of an irrotational correction $\boldsymbol{u}^{l+1} = \boldsymbol{u}^* - \nabla\phi$, leading to the following Poisson equation in the auxiliary variable

$$\nabla^2 \phi = \nabla \cdot \boldsymbol{u}^* \tag{16}$$

with homogeneous Neumann boundary conditions ($\partial\phi/\partial\boldsymbol{n} = 0$) where the velocity is prescribed, i.e., inlet and walls, and homogeneous Dirichlet boundary conditions ($\phi = 0$) at the outlet, if present. Then the pressure is updated as $p^{l+1} = p^l + \frac{\phi}{\Delta t}$ and the temperature is computed from the discretized energy equation (3):

$$\frac{3T^{l+1} - 4T^l + T^{l-1}}{2\Delta t} + \boldsymbol{u}^{l+1} \nabla T^{l+1} = C \nabla^2 T^{l+1} \tag{17}$$

3.2. Adaptive approach

The goal of the considered adaptive approach is to optimally increase the node density in such a way to reduce uniformly the truncation error over the whole domain. In other words, the higher the truncation error, the higher the node density at the next adaptive iteration. However, the estimation of the truncation error is difficult and expensive to compute and other error indicators are commonly used [23]. Up to now most adaptive approaches are based on some meaningful quantity related to the available solution, e.g., the gradient magnitude or curvature, and are not based on the actual truncation error. In this section we present two novel error indicators that can be used with the RBF-FD meshless method and which are based on the proper estimation of the truncation error obtained from the residual of the governing equations. More precisely, the residual can be chosen to be computed from either the momentum equation (2) or the energy equation (3), giving rise to what we have called the convection–diffusion (residual-based) error indicator. Otherwise, the residual can be chosen to be computed from the continuity equation (1), giving rise to what we have called the divergence (residual-based) error indicator. We also compare the proposed residual-based error indicators with a classical recovery-based error indicator which relies on the solution gradient. Error indicators are computed for each internal node and this information is used to locally update the spacing function according to the procedure presented in Section 3.2.4.

3.2.1. Convection–diffusion error indicator ("Mid1")

In the case of non-isothermal flows, the energy equation (3) can be considered to define the residual associated to the corresponding steady-state convection–diffusion operator $\mathcal{L}_{en}$ as follows:

$$\mathcal{L}_{en}T = \boldsymbol{u}\cdot\nabla T - \frac{1}{C}\nabla^2 T \tag{18}$$

At the steady-state, we have that $\mathcal{L}_{en}T^h = 0$ at the internal nodes because of the collocation approach of the RBF-FD method, while $\mathcal{L}_{en}T^h \neq 0$ elsewhere. The error indicator $\hat{e}_{en,k}$, based on such differential operator, is evaluated at the midpoints between each stencil center $\boldsymbol{x}_i$ and its k nearest neighbors by using the same RBF scheme employed for the discretization of the governing equations:

$$\hat{e}_{en,k}(\boldsymbol{x}_i) = \frac{1}{k}\sum_{\boldsymbol{x}_j\in S_k(\boldsymbol{x}_i)} |\mathcal{L}_{en}T^h(\boldsymbol{x}_{\frac{j}{2}})| \tag{19}$$

where $\boldsymbol{x}_{\frac{j}{2}} = (\boldsymbol{x}_i + \boldsymbol{x}_j)/2$ is the midpoint between nodes $\boldsymbol{x}_i$ and $\boldsymbol{x}_j$, and $S_k(\boldsymbol{x}_i)$ is the set of the k nearest nodes to the stencil center $\boldsymbol{x}_i$.

The same approach can be extended to isothermal flows by considering the momentum equation (2) to define the residual associated to the corresponding steady-state operator $\mathcal{L}^{(c)}_{mom}$ for each component u_c of the velocity $\boldsymbol{u} = (u_x, u_y, u_z)$:

$$\mathcal{L}^{(c)}_{mom}u_c = \boldsymbol{u}\cdot\nabla u_c - \frac{1}{A}\nabla^2 u_c + \frac{\partial p}{\partial c} - B\boldsymbol{z}_c, \quad c = x, y, z \tag{20}$$

In this case the error indicator is defined as follows:

$$\hat{e}_{mom,k}(\boldsymbol{x}_i) = \sqrt{\frac{1}{k}\sum_{\boldsymbol{x}_j\in S_k(\boldsymbol{x}_i)}\sum_{c=x,y,z}\left(\mathcal{L}^{(c)}_{mom}u^h_c(\boldsymbol{x}_{\frac{j}{2}})\right)^2} \tag{21}$$

We remark that this error indicator can also be used in the case of non-isothermal flows. We also remark that for the considered non-isothermal problems, the energy error indicator, Eq. (19), and the momentum error indicator, Eq. (21), should provide qualitatively similar results because the chosen Prandtl numbers are close to 1, and therefore the momentum and the energy equations share similar transport properties. For non-isothermal problems, we used the error indicator based on the energy equation, i.e., $\hat{e}_{en,k}$, while in the isothermal case we used the error indicator based on the momentum equation, i.e., $\hat{e}_{mom,k}$.

Investigations on the effect of the number k of nearest neighbors employed to compute these error indicators have shown a limited effect on the results. For this reason we have reported only the results obtained with $k = 1$ and we will refer to this residual-based error indicator as "Mid1". Finally, we observe that the computational cost for this error indicator is not negligible, requiring at least the same cost as the RBF-FD discretization of the corresponding convection–diffusion equation.

3.2.2. Divergence error indicator ("Div")

By considering the solution procedure presented in Section 3.1.3, we can define another error indicator based on the residual of the continuity equation (1):

$$\hat{e}_d(\boldsymbol{x}_i) = |\nabla\cdot\boldsymbol{u}^h(\boldsymbol{x}_i)| \tag{22}$$

In this case, it is not necessary to evaluate the residual of the continuity equation at points other than those of the node distribution since the employed solution procedure does not enforce the velocity field to be exactly divergence-free at the nodes. Therefore, the value of the divergence of the velocity at the nodes can be directly used as a suitable estimation of the continuity residual, and thus employed as error indicator. For this reason, this type of error indicator can be used only when the particular solution scheme presented in Section 3.1.3, based on a projection approach, is employed. It has to be noticed that the additional computation required for this error indicator is negligible since the RBF-FD divergence operator is already computed for the solution procedure. In what follows we will refer to this residual-based error indicator as "Div".

3.2.3. Gradient error indicator ("Grad")

The gradient error indicator, which is of recovery-based type, is based on the gradient of some flow variable F. In the case of a scalar variable F, the error indicator is defined as follows [7,19]:

$$\hat{e}_{gr,s}(\boldsymbol{x}_i) = \sqrt{\sum_{\boldsymbol{x}_j\in\bar{S}(\boldsymbol{x}_i)}\left(R[\nabla F^h](\boldsymbol{x}_j) - \nabla F^h(\boldsymbol{x}_j)\right)^2} \tag{23}$$

where F^h is the known approximation of F, $\bar{S}(\boldsymbol{x}_i)$ is the set of nodes of the stencil centered in $\boldsymbol{x}_i$ without the center $\boldsymbol{x}_i$ itself. The term $R[\nabla F^h]$ is defined as follows:

$$R[\nabla F^h](\boldsymbol{x}_j) = \frac{1}{m}\sum_{\boldsymbol{x}_k\in\bar{S}(\boldsymbol{x}_j)}\nabla F^h(\boldsymbol{x}_k) \tag{24}$$

In the case of a vector F with components (F_x, F_y, F_z), the gradient error indicator is defined as follows:

$$\hat{e}_{gr,v}(\boldsymbol{x}_i) = \sqrt{\sum_{\boldsymbol{x}_j\in\bar{S}(\boldsymbol{x}_i)}\sum_{c=x,y,z}\left(R[\nabla F^h_c](\boldsymbol{x}_j) - \nabla F^h_c(\boldsymbol{x}_j)\right)^2} \tag{25}$$

With the previous definitions, steep variations in the solution gradients lead to large values of the gradient error indicator. Similarly to the convection–diffusion error indicator, for the non-isothermal problems we used the scalar error indicator based on the temperature, i.e., $F = T$, while in the isothermal case we used the vector error indicator based on the velocity, i.e., $F = \boldsymbol{u}$. The computational effort required by this error indicator is fairly low because it requires only the evaluation of gradients at the meshless nodes, for which RBF-FD operators are already available. In the next sections we will refer to this gradient-based error indicator as "Grad".

3.2.4. Spacing function update

The proposed adaptive approach proceeds in an iterative fashion starting from a constant spacing function $s(\boldsymbol{x})$ over the whole domain.

Then, at each adaptive iteration, $s(\boldsymbol{x})$ is updated according to the chosen error indicator and a completely new node distribution is generated according to the procedure presented in Section 3.1.1. This strategy is different from the adaptive meshless approaches proposed in [13, 15–17] where new nodes are added to the existing ones. Despite not being an optimal technique, the chosen strategy remains highly fast and effective, as the employed node generation process is both fast and effective. The increase (or decrease) in the number of nodes between successive adaptive iterations is controlled by the nodal growth rate γ, defined by $N_I^{k+1} = \gamma N_I^k$ where N_I^k is the number of internal nodes at iteration k. Two values for γ are considered, namely $\gamma = 1$, i.e., constant number of nodes, and $\gamma = 1.5$, i.e., the number of nodes increases by 50% with each iteration. We observe that the actual increase in the number of nodes may differ from the target increase, therefore when the number of nodes is shown on a logarithmic scale, successive adaptive iterations are not exactly equidistant from each other.

Given a target number of internal nodes N_I^{k+1}, the spacing function is updated for each internal node $\boldsymbol{x}_i$ as follows:

$$s^{(k+1)}(\boldsymbol{x}_i) = \frac{\tau \cdot s^{(k)}(\boldsymbol{x}_i)}{\left(\tilde{e}^{(k)}(\boldsymbol{x}_i)\right)^{1/(P-1)}} \tag{26}$$

where $s^{(k)}$ is the spacing function at iteration k, $\tilde{e}^{(k)}$ is the smoothed error indicator at iteration k, P is the chosen polynomial degree for the RBF expansion and the constant τ is defined as follows in order to provide approximately the target number of internal nodes N_I^{k+1} at the next iteration:

$$\tau = \sqrt[3]{\frac{\sum_{\boldsymbol{x}_i \in X_I^{(k)}} \left(\tilde{e}^{(k)}(\boldsymbol{x}_i)\right)^{3/(P-1)}}{N_I^{k+1}}} \tag{27}$$

where $X_I^{(k)}$ is the set of all internal nodes at iteration k. Before being used in the spacing function update, equation (26), the error $\hat{e}^k$ needs to be smoothed because it can be very noisy. This noise mainly depends on the fact that the specific node arrangement within local stencils changes from node to node, and also on the fact that some error indicator is computed on a finite number of neighboring nodes, which again change from node to node. However, once the smoothing parameters are chosen appropriately, this noise is reduced without introducing numerical issues. The proper values for these free parameters can be problem dependent, e.g., they can depend upon the geometry, boundary conditions and flow regime. Therefore, some calibration is required, which can be a limitation in the general case. For the considered problems, the smoothing of the error $\hat{e}^k$ is done by means of 20 Laplacian smoothing iterations with under-relaxation parameter $\omega = 0.5$, producing the smoothed error $\tilde{e}^{(k)}$. Since at each adaptive iteration the spacing function is defined and updated only on internal nodes, the inverse distance weighting method with 8 nearest neighbors and power parameter $p = 4$ [41] is employed to interpolate the updated spacing function at each point required by the node generation procedure presented in Section 3.1.1.

A new adaptive iteration is started when the steady-state is reached, declared when:

$$\frac{|q^l - q^{l-1}|}{q^l} < 10^{-5} \tag{28}$$

where q^l is the reference integral quantity: Nusselt number Nu for the non-isothermal cases, drag coefficient C_d for the isothermal flow in a pipe, or Fanning friction factor f for the isothermal flow in the TPMS structure, at time level l.

4. Geometries and boundary conditions

4.1. Natural convection in a spherical shell

The domain is enclosed between two concentric spheres with radii r_1 and r_2 such that $r_2/r_1 = 5$ as shown in Fig. 1(a). The following boundary conditions are considered:

- no-slip condition on both spheres;
- $T = T_h$ on the internal sphere;
- $T = T_c$ on the external sphere.

By considering the gravitational acceleration g and a fluid with density ρ, kinematic viscosity ν, thermal diffusivity α and volumetric thermal expansion coefficient β, the governing equations are made nondimensional by considering the following reference scales: the inner sphere diameter $D = 2r_1$ for the length, $u_0 = \sqrt{g\beta D \Delta T}$ for the velocity, D/u_0 for the time, $\Delta T = T_h - T_c$ for the temperature and $\rho_0 u_0^2$ for the pressure. The Boussinesq approximation is employed to model buoyancy effects, i.e., the density in the buoyancy term has a linearized dependence on the temperature where $T_0 = (T_h + T_c)/2$ is the reference temperature at which the reference density ρ_0 is considered. The resulting dimensionless Eqs. (1)–(3) with $A = \sqrt{\mathrm{Ra}/\mathrm{Pr}}$, $B = T$ and $C = \sqrt{\mathrm{Ra} \cdot \mathrm{Pr}}$ are then expressed in terms of the Prandtl number $\mathrm{Pr} = \nu/\alpha$ and the Rayleigh number $\mathrm{Ra} = g\beta\Delta T D^3/(\nu\alpha) = u_0^2 D^2/(\nu\alpha)$. We considered a Prandtl number Pr = 0.71, representative of air, and two Rayleigh numbers, Ra = 500 and Ra = 1000, both corresponding to steady-state solutions. The temperature field in the case Ra = 1000 is shown in Fig. 1(b) for half of a vertical section of the domain.

4.2. Forced convection in a pipe with a spherical obstacle

The domain is a circular pipe of radius r_c and length $L = 5r_c$ containing a spherical obstacle of radius r_s with $r_c/r_s = 4$. The center of the sphere lies on the pipe axis at axial distance $\Delta x_s = L/4$ from the inlet, as shown in Fig. 2(a). The following boundary conditions are considered:

- inlet: parabolic velocity profile $u = u_0\left(1 - (r/r_c)^2\right)$ with maximum velocity u_0 at the center and $T = T_c$;
- circular pipe wall: no-slip condition and adiabaticity;
- spherical obstacle: no-slip condition and $T = T_h$;
- outlet: homogeneous Neumann boundary conditions for both velocity and temperature.

By considering a fluid with density ρ, kinematic viscosity ν and thermal diffusivity α, the governing equations are made nondimensional by considering the following reference scales: $D = 2r_s$ for the length, u_0 for the velocity, D/u_0 for time, $\Delta T = T_h - T_c$ for temperature and ρu_0^2 for pressure. Buoyancy effects are neglected. The resulting dimensionless Eqs. (1)–(3) with $A = \mathrm{Re}$, $B = 0$ and $C = \mathrm{Re} \cdot \mathrm{Pr}$ are then expressed in terms of the Prandtl number $\mathrm{Pr} = \nu/\alpha$ and the Reynolds number $\mathrm{Re} = (u_0 \cdot D)/\nu$. We considered a Prandtl number Pr = 1 and two Reynolds numbers Re = 100 and Re = 150, both corresponding to steady-state solutions. Figs. 2(b) and 2(c) show the temperature and the axial velocity fields for half of a section of the domain in the case Re = 150.

4.3. Isothermal flow in a pipe with a spherical obstacle

The domain and the boundary conditions for the velocity are the same as in the forced convection problem, Section 4.2, but the flow is isothermal. The dimensionless Eqs. (1)–(2) are now considered, with $A = \mathrm{Re}$ and $B = 0$. The considered Reynolds numbers are again Re = 100 and Re = 150.

4.4. Fully developed, isothermal flow in Schwarz-D TPMS structure

The domain is implicitly defined by the following level set equation which defines the solid walls:

$$s_x s_y s_z + s_x c_y c_z + s_y c_z c_x + s_z c_x c_y = 0 \tag{29}$$

where $c_t = \cos(\pi t/L)$, $s_t = \sin(\pi t/L)$ and L is the side length of the periodic cubic cell representing the smallest repeating module of the

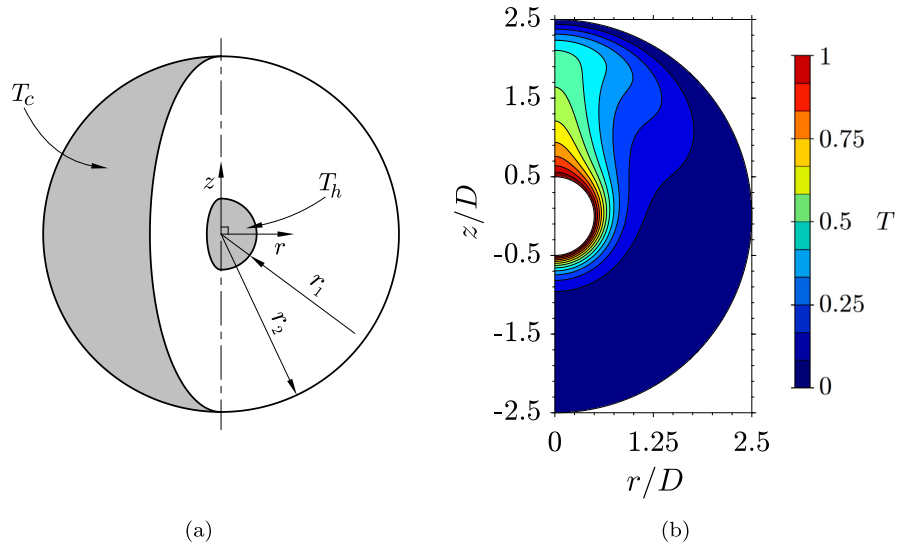

Fig. 1. Domain (a) and temperature (b) for the natural convection problem, Ra = 1000.

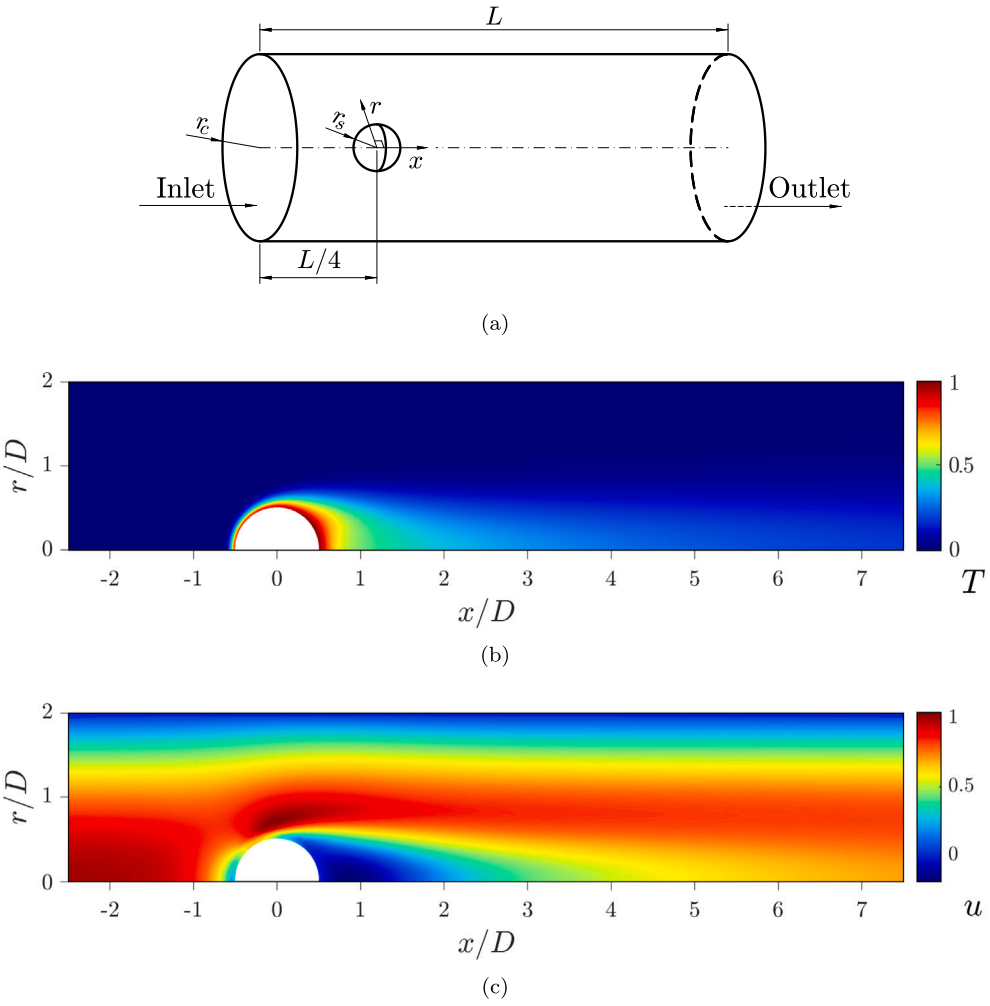

Fig. 2. Domain (a), temperature T (b) and axial velocity u (c) for the forced convection problem, Re = 150.

TPMS structure. A graphical representation of the Schwarz-D TPMS is shown in Fig. 3 together with an example of node distribution covering the computational domain. The geometric complexity of this domain provides additional insights into the features and advantages of the proposed adaptive approaches. The hydraulic diameter is defined by $d_H = 4V/A_S$ where $V = 0.5L^3$ is the fluid domain volume and $A_S = 3.85L^2$ is the wetted surface area. No-slip boundary conditions for the velocity are imposed at the walls, zero wall-normal derivative condition

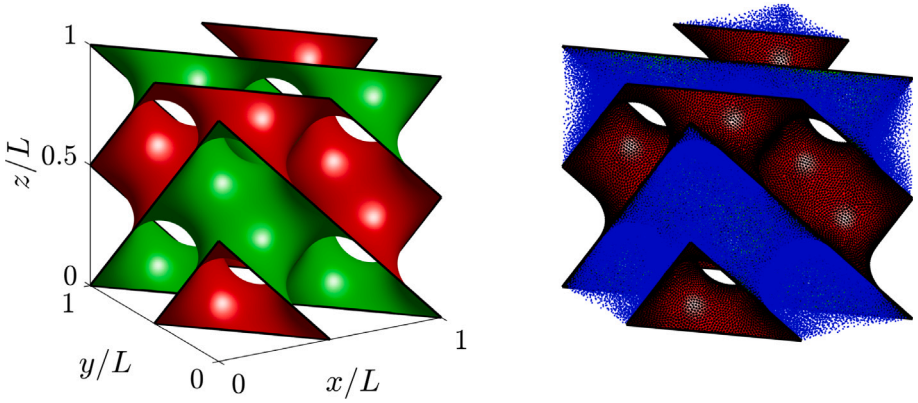

Fig. 3. Geometry (left) and an example of node distribution with $N = 2 \times 10^5$ nodes (right) for the Schwarz-D TPMS structure. Internal nodes are shown in blue, boundary nodes in black.

is enforced for the pressure and periodic conditions are then considered for both velocity and periodic pressure $\tilde{p}$ at the fluid boundaries of the periodic cell. By considering a fluid with density ρ and kinematic viscosity ν, the governing equations are made nondimensional by considering the following reference scales: hydraulic diameter d_H for the length, $u_0 = Q_V L/V$ for the velocity, taken as the volumetric average of the velocity u in the x direction with Q_V the volumetric flow rate, $t_0 = d_H/u_0$ for time and ρu_0^2 for the pressure. The resulting dimensionless Eqs. (1)–(3) with $A = \mathrm{Re}$ and $B = 0$ are then expressed in terms of the Reynolds number $\mathrm{Re} = u_0 d_H/\nu$. A detailed description of the problem can be found in [24]. We point out that in the considered case the streamwise pressure gradient β is fixed and the Reynolds number is obtained as a result. The chosen dimensionless pressure gradient is $\beta = 4.35$, corresponding to a Reynolds number $\mathrm{Re} \approx 210$.

5. Results

The effects of different error indicators and different parameters for the presented adaptive approach have been thoroughly investigated by performing several simulations for each of the considered fluid flow problems. For the considered axisymmetric problems, the accuracy and the convergence properties of the presented numerical approach are assessed by comparing the results with highly accurate 2D axisymmetric reference solutions obtained with two widely used mesh-based finite volume solvers, namely the industry-grade solver ANSYS Fluent (2024R1) and the open source solver OpenFOAM (v2012). Furthermore, infinite grid extrapolation with highly refined grids is performed on Fluent solutions in order to provide the most accurate reference solutions possible. In order to highlight the dependence also upon the employed RBF-FD discretization scheme, especially in the case of the residual-based error indicators, simulations are carried out for two polynomial degrees $P = 2$ and $P = 3$ for the first problem, i.e., natural convection in a spherical shell, while $P = 3$ is employed for the remaining problems.

5.1. Natural convection in a spherical shell

Fig. 4 shows, for each error indicator, the evolution of the Nusselt number for five adaptive iterations with $\gamma = 1$, i.e., the total number of nodes $N \approx 2 \times 10^5$ is kept almost constant. As previously stated, for this non-isothermal problem the energy equation is considered for the residual-based error indicator Mid1, while the temperature field is considered for the gradient error indicator. Results are reported for Rayleigh numbers $\mathrm{Ra} = 500$ and $\mathrm{Ra} = 1000$ and polynomial degree $P = 2$ and $P = 3$. We recall that the adaptive process starts from a uniform node distribution with constant spacing function, corresponding to adaptive iteration $k = 0$. Slight variations in these initial Nusselt numbers are due to the employed node generation algorithm, which has some random component.

From Fig. 4 it can be seen that the Nusselt number changes significantly in the first two adaptive iterations, after which it remains almost constant. This means that in this case, given a fixed number of nodes, two adaptive iterations are sufficient to obtain near-optimal node distributions and successive iterations do not lead to any improvement. Residual-based error indicators (Mid1 and Div) lead to similar results, while the gradient error indicator (Grad) leads to slightly larger differences from the reference Nu value in each case. The difference between residual-based error indicator and recovery-based error indicator is due to the fact that the first ones have a stronger numerical foundation, as already pointed out in [23]. Moreover, as expected, the results obtained with polynomial degree $P = 3$ are more accurate than those obtained with $P = 2$, especially when the residual-based error indicators are employed. We remark that the lack of convergence to the reference Nusselt number is only apparent since the nodal spacing does not decrease uniformly over the whole domain when $\gamma = 1$, i.e., when the number of nodes is kept almost constant with each adaptive iteration, but instead it decreases in some areas and increases in others.

Fig. 5 shows, for each error indicator, the convergence of the Nusselt number for five adaptive iterations with nodal growth rate $\gamma = 1.5$, i.e., the number of nodes increases by 50% with each iteration, again for Rayleigh numbers $\mathrm{Ra} = 500$ and $\mathrm{Ra} = 1000$ and polynomial degrees $P = 2$ and $P = 3$. The adaptive process is started from a uniform node distribution with $N \approx 10^5$ nodes. Convergence results for a non-adaptive strategy with uniform node distributions, i.e., $s(\boldsymbol{x}) = const$, are also shown for comparison ("Unif" in the figures). In all cases, as expected, already after the first adaptive iteration, the Nusselt numbers obtained with the adaptive approach are much closer to the reference values than the ones obtained with uniform node distributions. From the same figure it can also be seen that the adaptive approach provides very similar results in each case, regardless of the chosen error indicator. As expected, the convergence to the reference Nusselt number with $P = 2$ is slower than with $P = 3$, and the Nu values computed with the adaptive approach with $P = 2$ after one adaptive iteration are closer to the reference values than that obtained by using uniform node distributions with the largest number of nodes and $P = 3$.

Comparisons of Nusselt number with ANSYS Fluent and OpenFOAM are shown in Table 1, where 2D axisymmetric models with high quality structured grids have been considered. The wedge angle for the OpenFOAM grids is set to 5° and the buoyantBoussinesqSimpleFoam solver has been used. In order to provide a fair comparison of the performance of the different approaches, the number of 2D grid cells N_{2D} actually used for the computations is such that the equivalent number of axisymmetric 3D cells N_{3D} is approximately equal to the employed number of meshless nodes N. Convective fluxes are discretized with central differencing schemes in both Fluent and OpenFOAM to

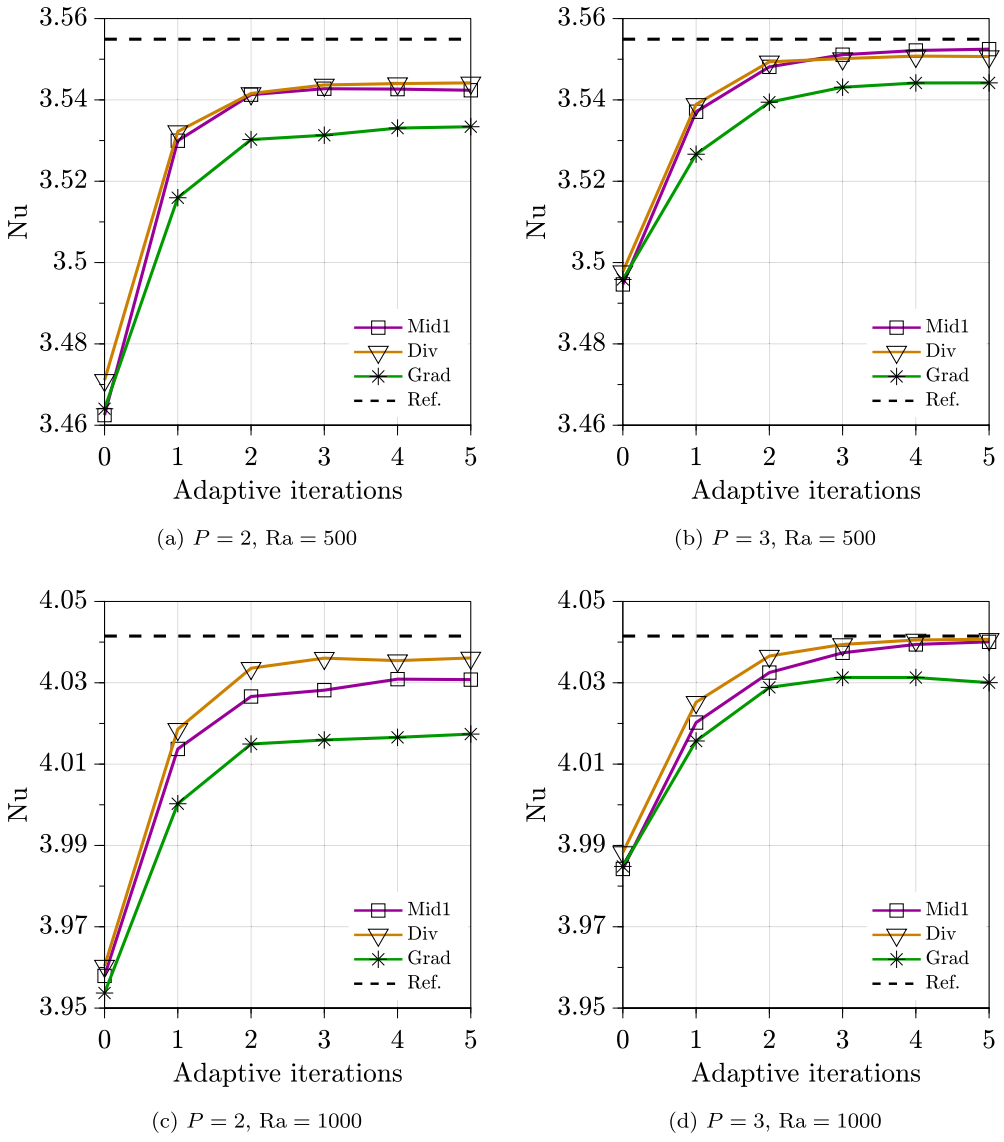

Fig. 4. Evolution of the Nusselt number in the natural convection problem, nodal growth rate $\gamma = 1$ (constant number of nodes $N \approx 2 \times 10^5$).

minimize numerical diffusion. In order to provide further insights on the convergence of the considered methods, two types of grids have been used: the first type of grid with uniform cell size along the radial direction (bias = 1), while in the second type of grid the cells are refined radially near the internal sphere (bias = 5) in order to accurately resolve boundary layers.

As it can be seen from Table 1, the trends are qualitatively similar for each approach, with all meshless results highlighting a slightly faster convergence to the reference values with respect to mesh-based results. We remark that the meshless results for $N \approx 10^5$ nodes are obtained on uniform node distributions, while we point out again that mesh-based results are obtained with high quality 2D structured grids. Despite the fact that the exact same meshes are employed for both OpenFOAM and Fluent, OpenFOAM results highlight monotonous increasing trends, while Fluent results highlight monotonous decreasing trends.

Fig. 6 shows the evolution of the node distribution with each adaptive iteration for both strategies $\gamma = 1$ and $\gamma = 1.5$ in the case Ra = 1000, $P = 2$ and the energy equation residual-based error indicator is used. For clarity only a small section of half of the domain is shown. As in the previous results, the initial node distribution at iteration $k = 0$ has $N \approx 2 \times 10^5$ nodes for $\gamma = 1$ and $N \approx 10^5$ nodes for $\gamma = 1.5$.

Table 1
Nusselt number comparison for the natural convection problem. $P = 3$ and $\gamma = 1.5$ for the meshless results. OF = OpenFOAM, Nu_∞ = Fluent infinite grid extrapolation.

$N \times 10^5$	Grad	Div	Mid1	bias = 1		bias = 5	
				OF	Fluent	OF	Fluent
	Ra = 500, $Nu_\infty = 3.5549$						
1.0	3.4537	3.4472	3.4508	3.5112	3.5802	3.5311	3.5728
1.6	3.5398	3.5451	3.5474	3.5388	3.5774	3.5414	3.5642
2.5	3.5517	3.5546	3.5544	3.5500	3.5695	3.5465	3.5599
3.4	3.5543	3.5550	3.5550	3.5531	3.5642	3.5497	3.5576
4.4	3.5547	3.5552	3.5552	3.5540	3.5604	3.5515	3.5564
5.5	3.5550	3.5551	3.5552	3.5542	3.5581	3.5529	3.5557
	Ra = 1000, $Nu_\infty = 4.0415$						
1.0	3.9495	3.9554	3.9463	4.0063	4.1105	4.0204	4.0743
1.6	4.0247	4.0301	4.0306	4.0403	4.0994	4.0297	4.0584
2.4	4.0375	4.0414	4.0413	4.0493	4.0781	4.0341	4.0508
3.3	4.0408	4.0429	4.0419	4.0485	4.0643	4.0365	4.0466
4.4	4.0414	4.0425	4.0420	4.0458	4.0547	4.0377	4.0444
5.5	4.0417	4.0422	4.0421	4.0437	4.0492	4.0384	4.0431

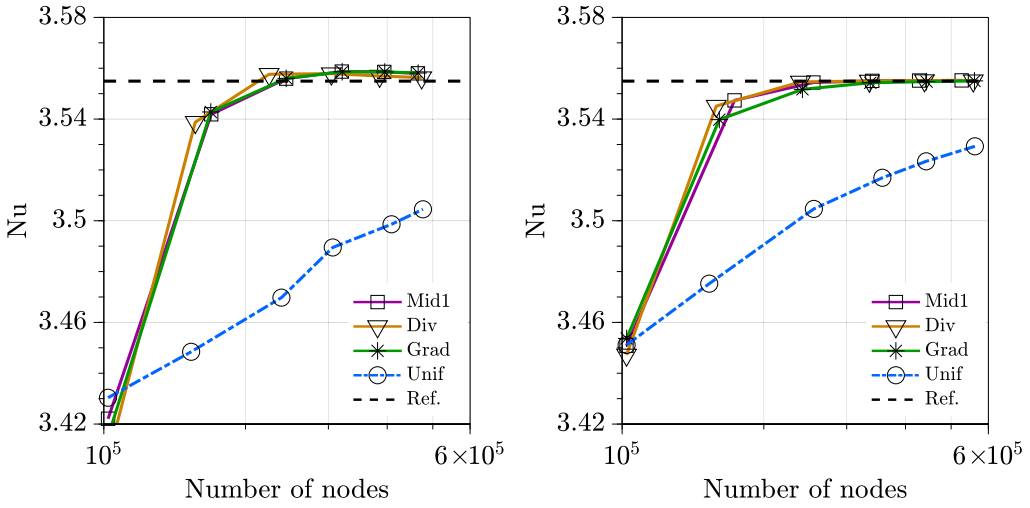

(a) Ra = 500, $P = 2$ (b) Ra = 500, $P = 3$

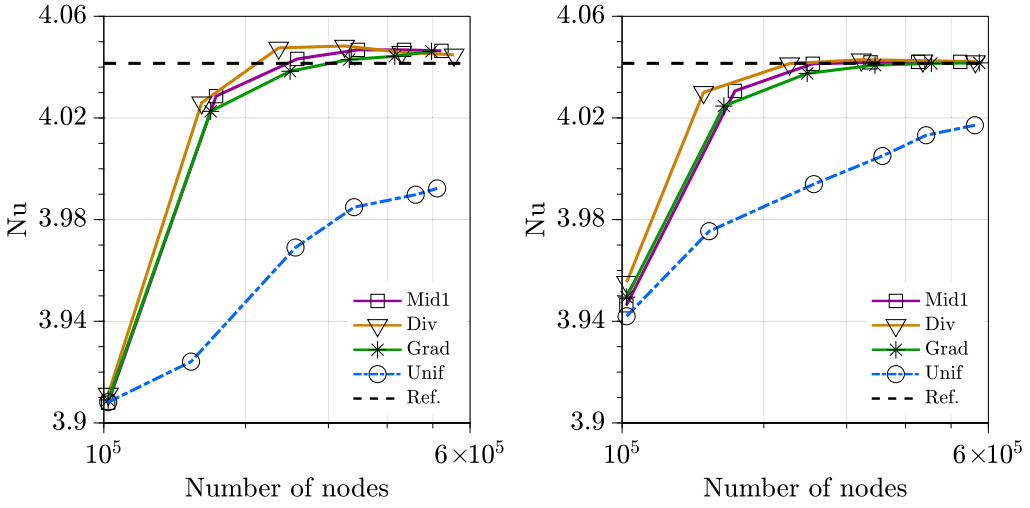

(c) Ra = 1000, $P = 2$ (d) Ra = 1000, $P = 3$

Fig. 5. Convergence curves for the Nusselt number in the natural convection problem, nodal growth rate $\gamma = 1.5$ (number of nodes increases by 50% with each iteration).

As expected, high node density is obtained around the inner sphere and in the upper part of the outer sphere where steep variations in the temperature field occur, i.e., thinner boundary layers. For this problem we also noticed that the evolution of the node distribution does not qualitatively change with the usage of different error indicators.

Since the results obtained with polynomial degree $P = 2$ are qualitatively similar to those with $P = 3$, in the next sections we decided to report only the results obtained with $P = 3$, which is also, to the best of the authors' experience, a good trade-off between accuracy and computational effort for these type of problems.

5.2. Forced convection in a pipe with a spherical obstacle

Fig. 7 shows, for each error indicator, the evolution of the Nusselt number for five adaptive iterations with $\gamma = 1$ ($N \approx 2.5\times10^5$ nodes) and $\gamma = 1.5$. The energy equation is considered for the residual-based error indicator Mid1, while the temperature field is again considered for the gradient error indicator. Results are reported for Reynolds numbers Re = 100 and Re = 150 and polynomial degree $P = 3$. The results for the initial (uniform) node distributions, as well as the convergence curves for the non-adaptive strategy with uniform node distributions, are not shown for clarity. Similarly to the natural convection problem, in the cases with $\gamma = 1$ in Figs. 7(a) and 7(c), the Nusselt number does not change significantly after the first two adaptive iterations. Residual-based error indicators (Mid1 and Div) lead again to similar results which are slightly different from those obtained with the gradient error indicator (Grad).

In the cases with $\gamma = 1.5$ in Figs. 7(b) and 7(d), it can be seen that the Nusselt numbers exhibit a rapid convergence to the reference value, although some lack of convergence appears for successive iterations in the case with Div error indicator. This behavior is probably due to some discontinuity in the smoothing or interpolation phases for the error indicator when the local nodal spacing becomes too small as a result of successive adaptive iterations.

The comparison of Nusselt numbers with ANSYS Fluent are summarized in Table 2, where again, similar to the previous problem, two types of grids with a different radial distribution of cell sizes, i.e., uniform (bias = 1) and refined near the internal sphere (bias = 5), are employed to better highlight the effects of cell size distribution on the convergence of a classical finite volume approach. Contrary to the previous natural convection problem, for this forced convection problem the Fluent results obtained with refined grids (bias = 5) highlight a faster convergence to the reference values than all meshless results. This difference could be due to the thin thermal and dynamic

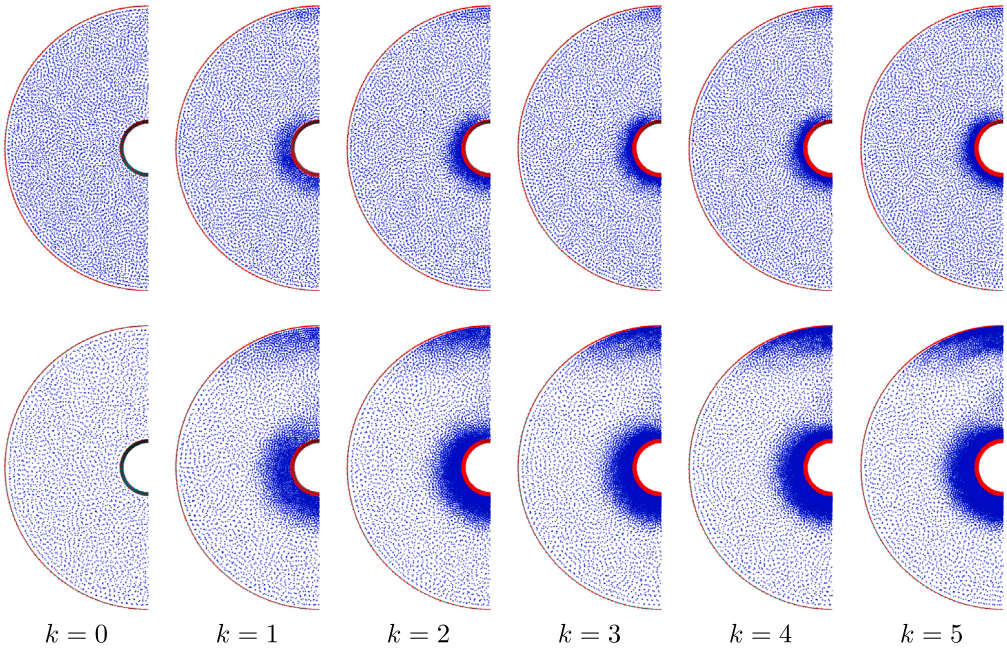

Fig. 6. Adaptive evolution (left to right) of the node distribution in a vertical section of the domain in the natural convection problem. Ra = 1000, $P = 2$, energy equation residual-based error indicator. Top row: nodal growth rate $\gamma = 1$ (constant number of nodes); bottom row: $\gamma = 1.5$ (number of nodes increases by 50% with each iteration). Boundary nodes are depicted in red, internal nodes in blue.

Table 2
Nusselt number comparison for the forced convection problem. $P = 3$ and $\gamma = 1.5$ for the meshless results. Nu_∞ = Fluent infinite grid extrapolation, b1 and b5 stand for grid bias = 1 and grid bias = 5.

$N\times10^5$	Grad	Div	Mid1	Fluent		Grad	Div	Mid1	Fluent	
				b1	b5				b1	b5
	Re = 100, Nu_∞ = 7.617					Re = 150, Nu_∞ = 8.929				
1.5	8.029	7.982	7.929	7.662	7.614	9.390	9.602	9.229	8.915	8.934
2.1	7.729	7.599	7.586	7.688	7.615	9.323	9.139	8.907	8.991	8.934
3.0	7.600	7.585	7.596	7.697	7.616	8.935	8.908	8.911	9.030	8.934
3.8	7.602	7.593	7.596	7.696	7.617	8.909	8.920	8.915	9.046	8.934
4.7	7.602	7.570	7.600	7.690	7.617	8.914	8.906	8.916	9.048	8.933
5.4	7.600	7.513	7.602	7.681	7.617	8.913	8.751	8.918	9.044	8.933

boundary layers appearing at the front of the internal sphere (see Fig. 2(b)) which would require even more refined and/or anisotropic node distributions to be accurately resolved. This fact is also confirmed by the fact that Fluent results obtained with radially uniform grids (bias = 1) show very slow convergence to reference values.

Fig. 8 shows the evolution of node distributions with each adaptive iteration for different error indicators. The node distributions obtained by using residual-based error indicators Mid1 and Div are very similar, with an increase in the node density around the sphere which is more pronounced in the frontal part, as expected. The gradient error indicator, instead, leads to increased node density even along the wake behind the sphere: this means that, for the same number of nodes, node density around the sphere is lower with Grad error indicator than with Mid1 and Div error indicators. This in turn explains the slower convergence observed with the gradient error indicator, since most of the truncation error is limited to the thin boundary layer around the sphere. This finding is in perfect agreement with those of Roy [23], which highlighted that gradient-based adaptivity is not optimal for reducing the overall truncation error.

Fig. 9 shows the distributions of the relative error of local Nusselt number Nu_θ with respect to the reference values obtained with ANSYS Fluent as functions of the polar angle θ at the surface of the sphere ($\theta = 0$ at the front of the sphere, $\theta = \pi$ at the back) for different adaptive iterations k with $\gamma = 1.5$. Since the problem is solved in its 3D formulation, Nu values shown in Fig. 9 are averaged along the azimuthal direction, i.e., along circumferences perpendicular to the pipe axis. From these figures it is possible to appreciate the effectiveness of the adaptive approach in the uniform reduction of the error, especially during the first iterations. As already observed, Mid1 and Div error indicators lead to similar trends in error reduction, in the first adaptive iteration, while the gradient error indicator leads to slightly different trends. From the iteration $k = 3$ the error is very similar among all the error indicators with a good reduction of the error. At the adaptive iteration $k = 5$ with the Div error indicator some irregularities appear when $\theta < \pi/4$. This fact is in perfect agreement with the divergence present in figure Fig. 7, where the Nusselt number computed using the Div error indicator is diverging from the exact at the last adaptive iteration. From the Nu_θ distribution of Fig. 9(b) it can be observed that, as previously pointed out, such instabilities arise at the front of the sphere where the local spacing after 5 adaptive iterations becomes very small. As noted in Fig. 7, the other error indicators seem to avoid the onset of such instabilities.

5.3. Isothermal flow in a pipe with a spherical obstacle

Fig. 10 shows, for each error indicator, the evolution of the drag coefficient of the sphere C_d for five adaptive iterations with $\gamma = 1$ ($N \approx 2.5 \times 10^5$ nodes) and $\gamma = 1.5$. Results are reported for Reynolds numbers Re = 100 and Re = 150, and polynomial degree $P = 3$. For this isothermal problem the momentum equation is considered for the residual-based error indicator Mid1, while the velocity field is considered for the gradient error indicator.

In the case with $\gamma = 1$, Figs. 10(a) and 10(c), higher variations of C_d occur during the first two adaptive iterations, especially for the error indicators Mid1 and Div, similarly to what was observed for the Nu number in the previous problems. However, in this case the curves show some sort of apparent convergence towards the reference value even if the adaptive process with $\gamma = 1$, i.e., constant number of nodes, cannot be considered a convergent discretization process since the nodal spacing does not decrease uniformly, as already pointed out. Also in this case, we note that Mid1 and Div residual-based error indicators lead to very similar results, while the gradient error indicator highlights

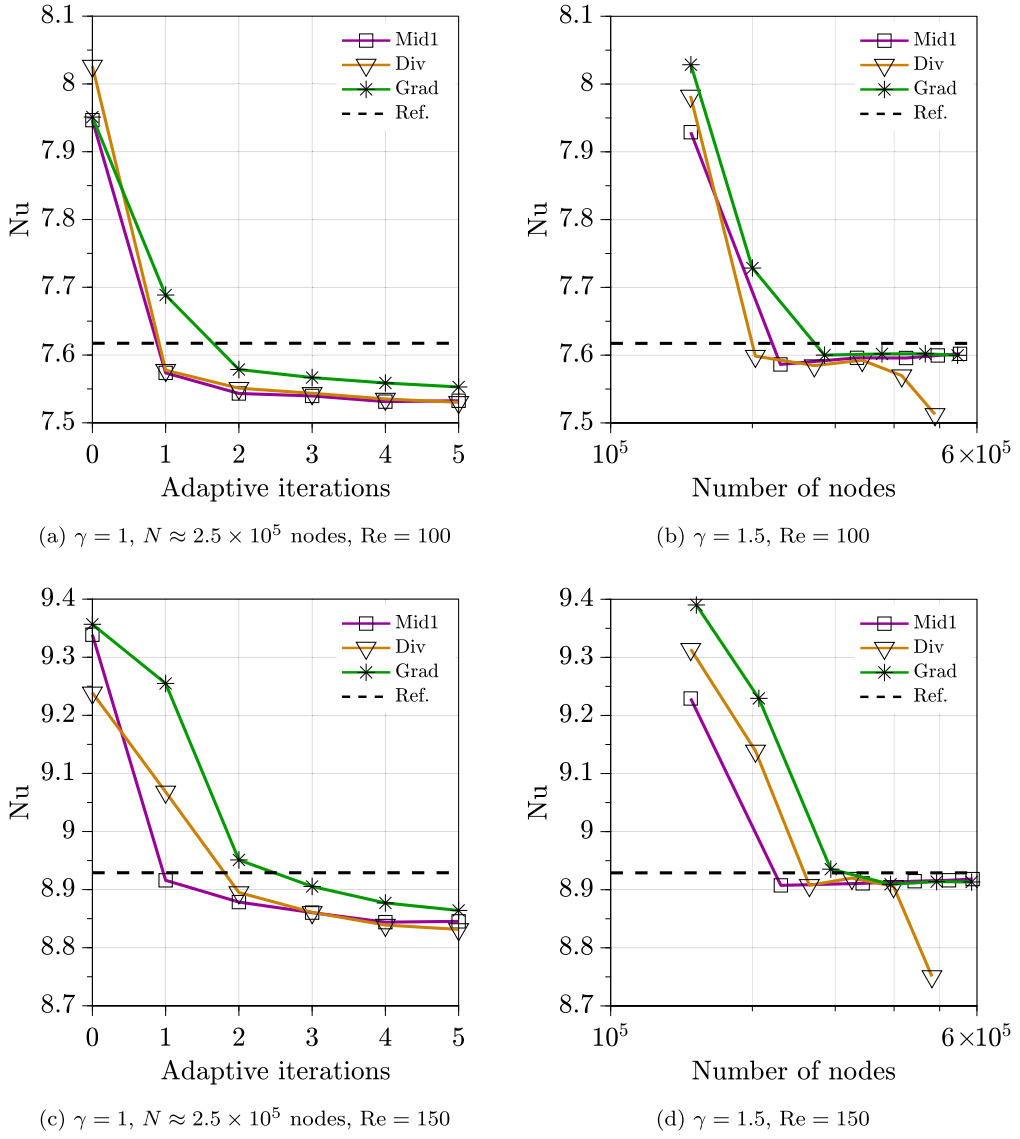

Fig. 7. Evolution of the Nusselt number in the forced convection problem. Left column, (a) and (c): nodal growth rate $\gamma = 1$ (constant number of nodes); right column, (b) and (d): $\gamma = 1.5$ (number of nodes increases by 50% with each iteration).

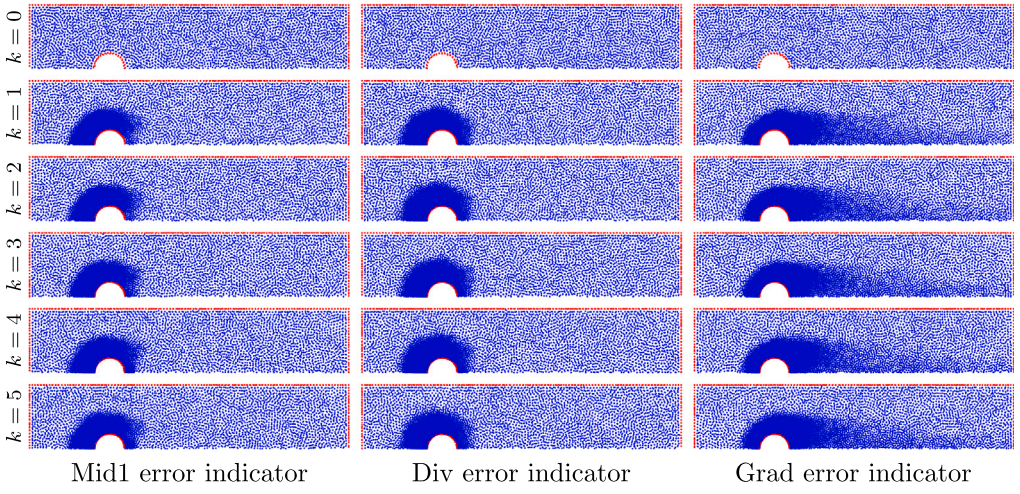

Fig. 8. Adaptive evolution (top to bottom) of the node distribution in an axial slice of the domain in the forced convection problem. Re = 150, nodal growth rate $\gamma = 1.5$ (number of nodes increases by 50% with each iteration). Each column refers to a different error indicator which drives the adaptivity. Boundary nodes are depicted in red, internal nodes in blue.

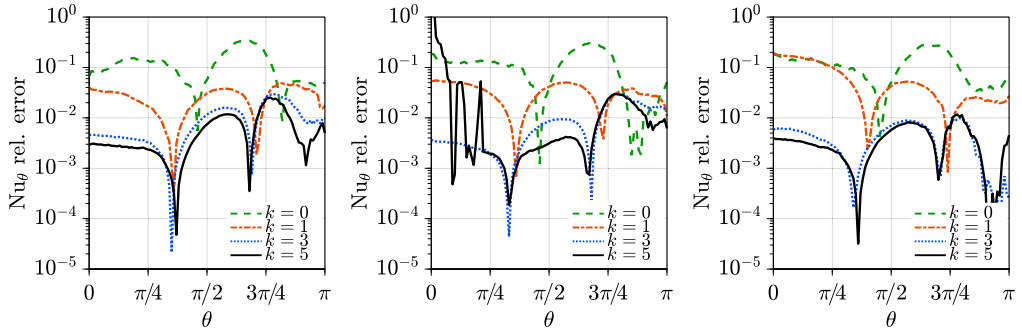

(a) Mid1 error indicator (b) Div error indicator (c) Grad error indicator

Fig. 9. Relative error of local Nusselt number Nu_θ along the polar angle θ of the sphere in the forced convection problem, nodal growth rate $\gamma = 1.5$ (number of nodes increases by 50% with each iteration), Re = 150.

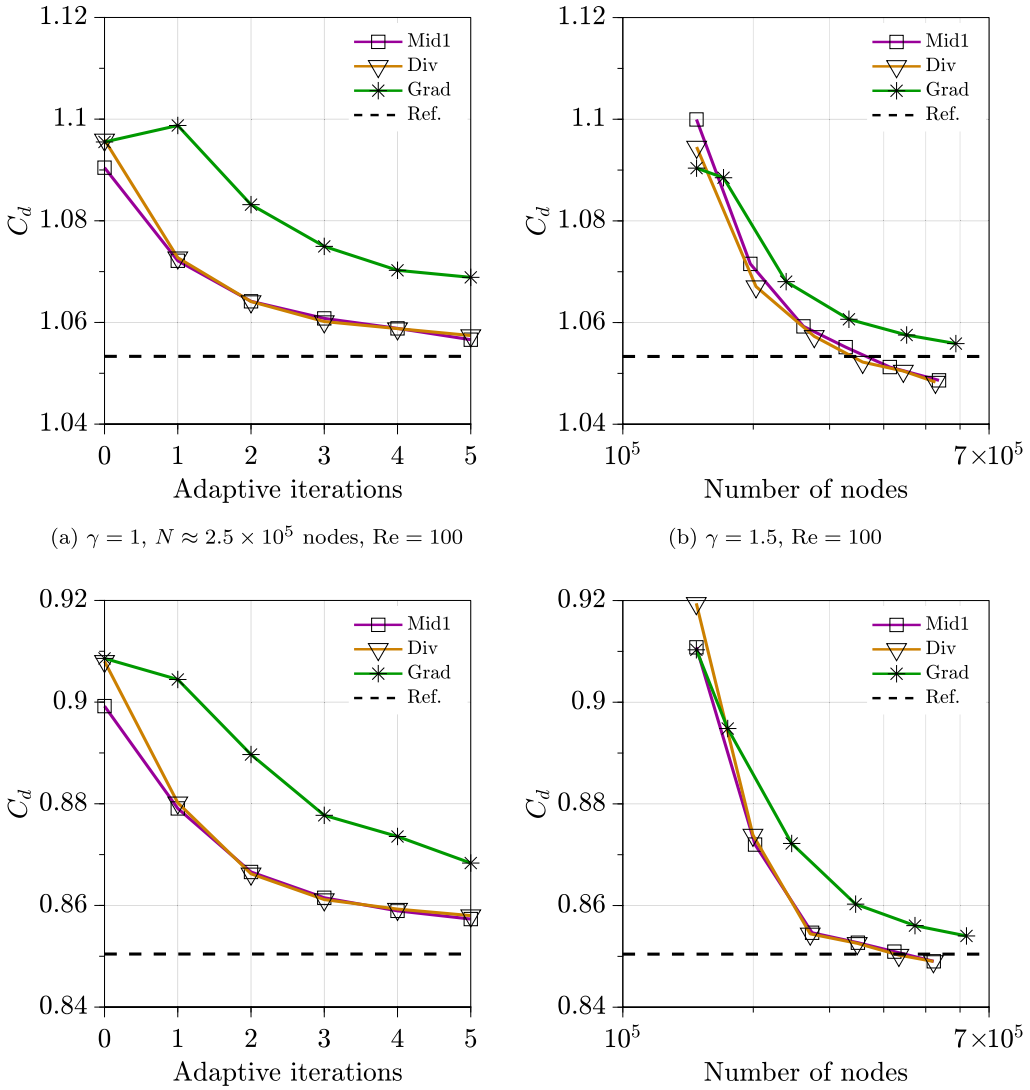

(a) $\gamma = 1$, $N \approx 2.5 \times 10^5$ nodes, Re = 100 (b) $\gamma = 1.5$, Re = 100

(c) $\gamma = 1$, $N \approx 2.5 \times 10^5$ nodes, Re = 150 (d) $\gamma = 1.5$, Re = 150

Fig. 10. Evolution of the drag coefficient in the isothermal flow problem. Left column, (a) and (c): nodal growth rate $\gamma = 1$ (constant number of nodes); right column, (b) and (d): $\gamma = 1.5$ (number of nodes increases by 50% with each iteration).

a slower convergence with larger differences from the reference C_d value. Moreover it can be noted that for both the Reynolds numbers the Grad error indicator does not lead to significant improvement in the C_d value at the first adaptive iteration, Figs. 10(a) and 10(c). This fact may be due to a significant difference in the node distributions generated by using such error indicator, Fig. 11. Similar trends are obtained with $\gamma = 1.5$, in Figs. 10(b) and 10(d), where Mid1 and Div error indicators lead to similar behaviors with a rapid convergence to the reference C_d

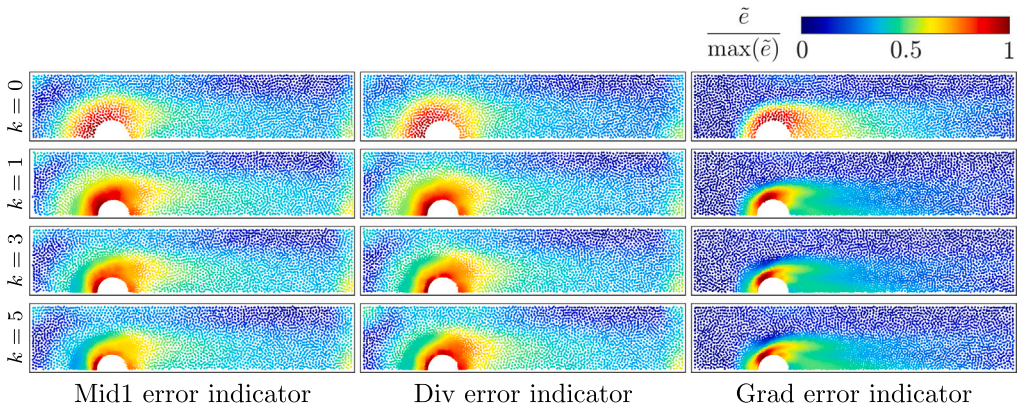

Fig. 11. Adaptive evolution (top to bottom) of the node distribution in an axial slice of the domain in the isothermal flow problem. Re = 150, nodal growth rate $\gamma = 1.5$ (number of nodes increases by 50% with each iteration). Each column refers to a different error indicator which drives the adaptivity. Nodes are colored by using the normalized value of the respective smoothed error indicator.

Table 3
Drag coefficient comparison for the isothermal flow problem. $P = 3$ and $\gamma = 1.5$ for the meshless results. $C_{d,\infty}$ = Fluent infinite grid extrapolation, b1 and b5 stand for grid bias = 1 and grid bias = 5.

$N\times10^5$	Grad	Div	Mid1	Fluent		Grad	Div	Mid1	Fluent	
				b1	b5				b1	b5
	Re = 100, $C_{d,\infty} = 1.053$					Re = 150, $C_{d,\infty} = 0.850$				
1.5	1.090	1.068	1.100	1.052	1.054	0.910	0.919	0.911	0.860	0.856
1.9	1.088	1.067	1.072	1.053	1.052	0.895	0.874	0.872	0.862	0.854
2.6	1.068	1.057	1.059	1.052	1.052	0.872	0.854	0.855	0.861	0.855
3.4	1.061	1.052	1.055	1.053	1.052	0.860	0.853	0.853	0.860	0.852
4.4	1.058	1.050	1.051	1.056	1.052	0.856	0.850	0.851	0.857	0.851
5.5	1.056	1.048	1.049	1.058	1.052	0.854	0.849	0.849	0.858	0.851

value, while the gradient error indicator shows a slower convergence, confirming once more that gradient-based adaptivity is not optimal.

Comparisons of drag coefficients with ANSYS Fluent are reported in Table 3 by using the same grids employed for the forced convection problem. Similar to the previous problem, Fluent results with refined grids (bias = 5) show a faster convergence to the reference values than meshless results, while Fluent results with uniform grids (bias = 1) exhibit again a slow convergence. These behaviors are again due to the thin dynamic boundary layer occurring at the surface of the internal sphere which requires anisotropic node distributions to be solved more accurately and efficiently. Once again, we emphasize that Fluent results are obtained with high quality 2D structured grids, which lead to very accurate results.

It has to be noticed that the error indicators used for this problem can be applied also to the non-isothermal problem in Section 4.2, with Grad and Mid error indicators that are referred to the velocity field instead of the temperature field. The Div error indicator is the same for both the problems and it can be seen that the lack of convergence highlighted in Figs. 7(b) and 7(d) in the evaluation of the Nusselt number does not seem to occur in the evaluation of the drag coefficient C_d. This mismatch may be due to the fact that the evaluation of the Nusselt number depends only on temperature gradients at the surface of the sphere, while the drag coefficient depends both on the shear stress, which in turn depends on the velocity gradients, and on the pressure. In the latter case, the numerical issues involved in evaluating boundary gradients at very small nodal spacings could be partially hidden by the pressure component.

Fig. 11 shows the evolution of the node distributions for each error indicator in the case $\gamma = 1.5$ and Re = 150. Nodes are colored by using the corresponding smoothed error indicators, normalized with respect to the maximum value over the whole domain. Similarly to the non-isothermal case, the residual-based error indicators lead to an increased node density around the sphere only, while the gradient error indicator leads to an increase in node density along the wake as well. Moreover, in the case of Mid1 error indicator, it can be noticed that the error field decreases noticeably around the sphere, highlighting the effectiveness of the convection–diffusion error indicator in the optimal reduction of the overall error, while it does not decrease equally clearly with Div and Grad indicators. In the latter case, already after the first adaptive iteration, a clearly visible spot with large errors appears, and successive iterations are unable to reduce this error. Therefore, the adaptive process driven by the velocity gradient alone does not seem the best choice for the optimal reduction of the overall error.

5.4. Isothermal, fully developed flow in Schwarz-D TPMS structure

Fig. 12(a) shows, for each error indicator, the evolution of the Fanning friction factor f (see [24] for further details) for five adaptive iterations with $\gamma = 1.5$ and polynomial degree $P = 3$. Similarly to the previous isothermal problem, the momentum equation is considered for the residual-based error indicator Mid1, while the velocity field is considered for the gradient error indicator. Contrary to the previous cases, Mid1 and Grad error indicators show similar convergence behavior, which is slightly slower than that of the Div error indicator. This difference is probably due to the different nature of the considered problems: in the previous cases the largest variations in the flow fields were limited to small regions (thin boundary layers) as opposed to the present case where the flow is fully developed, although confined by intricate geometry. Fig. 12(b) shows the evolution of the different normalized volume-averaged error indicators throughout the adaptive process for $\gamma = 1.5$. The normalized volume-averaged error indicator is computed by averaging the error indicator over the whole domain, normalized with respect to the corresponding maximum value along the adaptive process. Mid1 and Div error indicators highlight similar monotonous decrease, although the Div indicator starts with an almost zero error for $k = 0$ due to the uniform initial distribution. On the other hand, the Grad error indicator remains almost constant for the first three adaptive iterations, and then decreases.

Fig. 13 shows, for each error indicator, the adaptive evolution of the smoothed error indicator at the walls. The Mid1 indicator is able to uniformly and effectively reduce the error already from the first iteration, leading to an almost constant error for adaptive iteration $k = 3$, confirming the trend reported in Fig. 12(b). The wall distribution of the initial ($k = 0$) Mid1 error is very similar to that of the Div indicator at the next ($k = 1$) adaptive iteration, as are the corresponding errors for the subsequent iterations. On the other hand, the Grad indicator leads to error stagnation for the first three adaptive iterations, as already noted, although the error distribution for $k = 3$ is significantly smoother than the initial one.

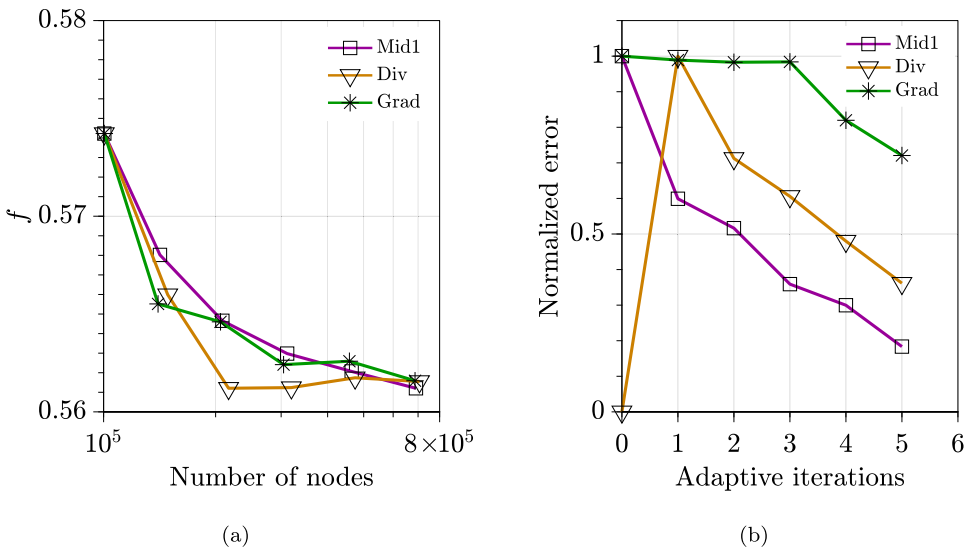

Fig. 12. Evolution of (a) Fanning friction factor f and (b) normalized volume-averaged error indicator for the fully developed flow in Schwarz-D TPMS structure, nodal growth rate $\gamma = 1.5$.

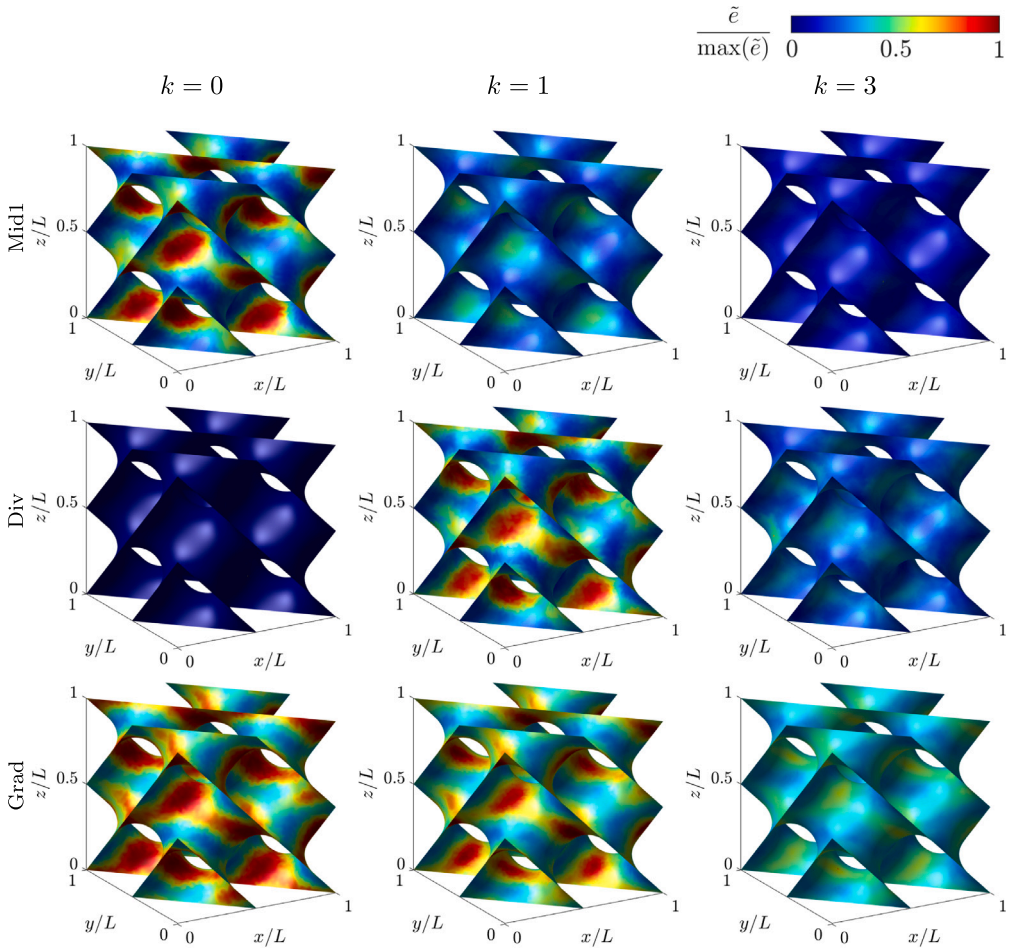

Fig. 13. Adaptive evolution (left to right) of the normalized smoothed error indicators at the walls for the fully developed flow in Schwarz-D TPMS structure, nodal growth rate $\gamma = 1.5$ (number of nodes increases by 50% with each adaptive iteration k). Each row refers to a different error indicator which drives the adaptivity.

The adaptive evolution of the wall spacing function is shown in Fig. 14 for each error indicator, starting from $k = 1$ since the initial ($k = 0$) spacing is constant. The larger differences in the distributions are encountered after the first adaptive iteration, i.e., $k = 1$, while the differences gradually decrease in the subsequent adaptive iterations. At the last ($k = 5$) adaptive iteration, the spacing distributions are surprisingly similar, as confirmed by the corresponding similar values of the Fanning friction factor in Fig. 12(a).

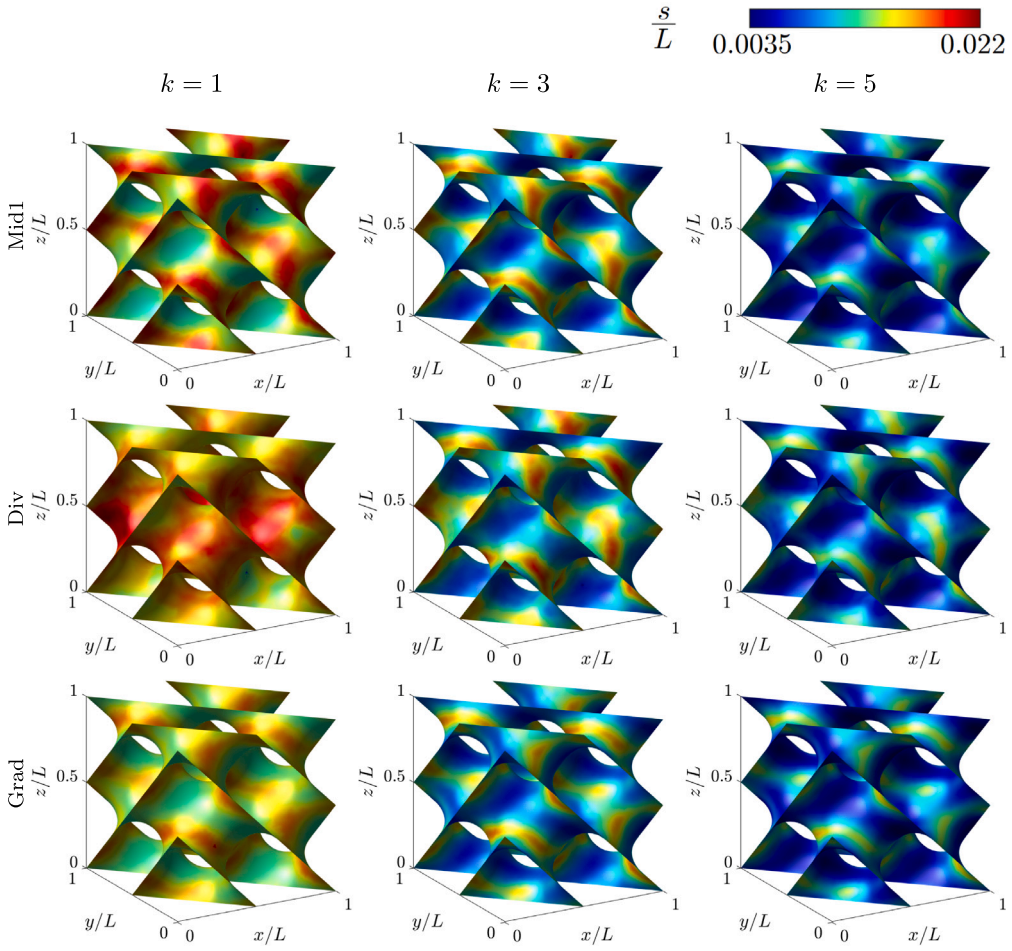

Fig. 14. Adaptive evolution (left to right) of the spacing function s at the walls for the fully developed flow in Schwarz-D TPMS structure, nodal growth rate $\gamma = 1.5$ (number of nodes increases by 50% with each adaptive iteration k). Each row refers to a different error indicator which drives the adaptivity. Constant spacing function is considered for the initial distribution $k = 0$.

6. Conclusions

In this paper we propose and compare different techniques for the adaptive solution of 3D fluid flow and heat transfer problems by using the RBF-FD meshless method. The goal of the considered adaptive process is to appropriately increase the node density so as to reduce the overall discretization error as uniformly as possible over the computational domain (h-adaptivity). Three different error indicators have been considered as error metrics to drive the adaptivity. Two error indicators are based on the residual of the governing equations, i.e., mass, momentum and energy conservation balances, while the third one is a traditional recovery-based error indicator that relies on solution gradients.

To the best of the authors' knowledge, this is the first time that such adaptive approaches are applied to the RBF-FD meshless solution of 3D fluid flow and heat transfer problems. Four steady-state laminar problems have been considered: a natural convection problem in a spherical shell, a forced convection problem in a circular pipe with a spherical obstacle, an isothermal fluid flow problem on the same domain and a fully developed flow problem in Schwarz-D triply periodic minimal surface (TPMS) structure. Numerical investigations highlighted that residual-based error indicators usually perform better than the gradient-based one in uniformly reducing the overall error, as predicted by the theory. Residual-based indicators, indeed, aim to approximate the truncation error which is the most appropriate metric to drive adaptivity. Nonetheless, modest differences are found in the considered cases, and this justifies the fact that the gradient-based error indicator is the most common choice in many commercial (mesh-based) CFD solvers, due also to its generality, low computational effort and ease of implementation. However, residual-based error indicators can be expected to be the most appropriate choice in the case of high-order meshless methods where the proper estimation of the truncation error is essential in order to ensure an optimal adaptive process. It has to be noticed that the Div error indicator does not require any additional computation as it directly utilizes results from the solution process. The gradient error indicator requires some limited additional computation, but it does not depend on the governing equations. In contrast, the Mid error indicator requires the evaluation of all the differential operators involved in the PDEs at the midpoints, thereby increasing the computational effort. Moreover, this adaptive approach and its use in conjunction with residual-based error indicators have general applicability and can be easily extended to a wide range of fluid flow and heat transfer problems of practical interest. An indirect limitation of the present meshless approach is connected to the fact that isotropic node distributions are employed. Indeed, such node distributions are not optimal for the efficient solution of fluid flow problems with practical interest where thin boundary layers must be accurately solved. Nonetheless, the proposed adaptive strategy can be appropriately extended to the case with anisotropic node distributions, with the resulting additional advantages, as well as to a wider range of fluid flow problems. Further research can also be conducted by investigating suitable combinations of the basic error indicators in order to combine their advantages and strengths.

CRediT authorship contribution statement

Luca Bacer: Writing – original draft, Visualization, Software, Methodology, Investigation, Formal analysis, Data curation, Conceptualization. **Riccardo Zamolo:** Writing – original draft, Visualization, Supervision, Methodology, Investigation, Conceptualization. **Davide Miotti:** Writing – original draft, Supervision, Software. **Enrico Nobile:** Writing – original draft, Supervision, Project administration, Funding acquisition, Conceptualization.

Declaration of competing interest

The authors declare that they have no known competing financial interests or personal relationships that could have appeared to influence the work reported in this paper.

Acknowledgments

This study was carried out within the "WADERE - Development of thermally-driven sorption process for WAtER DEsAlinAtion using low-grade REnEWAblE EnERgy (2022PSPA8R)" project – funded by the Ministero dell'Università e della Ricerca, Italy – within the PRIN 2022 program (D.D. 104 - 2/2/2022). This manuscript reflects only the authors' views and opinions and the Ministry cannot be considered responsible for them.

Data availability

Data will be made available on request.

References

[1] Liu GR. Meshfree Methods: Moving Beyond the Finite Element Method. CRC Press; 2009, http://dx.doi.org/10.1201/9781420082104.
[2] Li H, Mulay S. Meshless Methods and Their Numerical Properties. CRC Press; 2013, http://dx.doi.org/10.1201/b14492.
[3] Fornberg B, Flyer N. Fast generation of 2-D node distributions for mesh-free PDE discretizations. Comput Math Appl 2015;69(7):531–44. http://dx.doi.org/10.1016/j.camwa.2015.01.009.
[4] Slak J, Kosec G. On generation of node distributions for meshless PDE discretizations. SIAM J Sci Comput 2019;41(5):A3202–29. http://dx.doi.org/10.1137/18m1231456.
[5] Zamolo R, Nobile E. Two algorithms for fast 2D node generation: Application to RBF meshless discretization of diffusion problems and image halftoning. Comput Math Appl 2018;75(12):4305–21. http://dx.doi.org/10.1016/j.camwa.2018.03.031.
[6] Shankar V, Kirby R, Fogelson A. Robust node generation for mesh-free discretizations on irregular domains and surfaces. SIAM J Sci Comput 2018;40:A2584–608. http://dx.doi.org/10.1137/17M114090X.
[7] Slak J. Adaptive RBF-FD method (Ph.D. thesis), University of Ljubljana; 2020, URL https://e6.ijs.si/~jslak/files/phd.pdf.
[8] Carey GF, Humphrey DL. Mesh refinement and iterative solution methods for finite element computations. Internat J Numer Methods Engrg 1981;17(11):1717–34. http://dx.doi.org/10.1002/nme.1620171110.
[9] Berger MJ, Oliger J. Adaptive mesh refinement for hyperbolic partial differential equations. J Comput Phys 1984;53(3):484–512. http://dx.doi.org/10.1016/0021-9991(84)90073-1.
[10] Loehner R. An adaptive finite element scheme for transient problems in CFD. Comput Method Appl M 1987;61(3):323–38. http://dx.doi.org/10.1016/0045-7825(87)90098-3.
[11] Frey P, Alauzet F. Anisotropic mesh adaptation for CFD computations. Comput Method Appl M 2005;194(48):5068–82. http://dx.doi.org/10.1016/j.cma.2004.11.025.
[12] Baker TJ. Mesh adaptation strategies for problems in fluid dynamics. Finite Elem Anal Des 1997;25(3):243–73. http://dx.doi.org/10.1016/S0168-874X(96)00032-7.
[13] Angulo A, Pozo LP, Perazzo F. A posteriori error estimator and an adaptive technique in meshless finite points method. Eng Anal Bound Elem 2009;33(11):1322–38. http://dx.doi.org/10.1016/j.enganabound.2009.06.004.
[14] Afshar M, Naisipour M, Amani J. Node moving adaptive refinement strategy for planar elasticity problems using discrete least squares meshless method. Finite Elem Anal Des 2011;47(12):1315–25. http://dx.doi.org/10.1016/j.finel.2011.07.003.
[15] Davydov O, Oanh DT. Adaptive meshless centres and RBF stencils for Poisson equation. J Comput Phys 2011;230(2):287–304. http://dx.doi.org/10.1016/j.jcp.2010.09.005.
[16] Kosec G, Šarler B. H-adaptive local radial basis function collocation meshless method. CMC- Comput Mater Con 2011;26(3):227–54. http://dx.doi.org/10.3970/cmc.2011.026.227.
[17] Oanh DT, Davydov O, Phu HX. Adaptive RBF-FD method for elliptic problems with point singularities in 2D. Appl Math Comput 2017;313:474–97. http://dx.doi.org/10.1016/j.amc.2017.06.006.
[18] Slak J, Kosec G. Adaptive RBF-FD method for Poisson's equation. WIT Trans Eng Sci 2019;126:149–57. http://dx.doi.org/10.2495/BE420131.
[19] Hu W, Trask NA, Hu X, Pan W. A spatially adaptive high-order meshless method for fluid–structure interactions. Comput Method Appl M 2019;355. http://dx.doi.org/10.1016/j.cma.2019.06.009.
[20] Fornberg B, Flyer N. A Primer on Radial Basis Functions with Applications to the Geosciences. Society for Industrial and Applied Mathematics; 2015, http://dx.doi.org/10.1137/1.9781611974041.
[21] Fornberg B, Flyer N. Solving PDEs with radial basis functions. Acta Numer 2015;24:215–58. http://dx.doi.org/10.1017/S0962492914000130.
[22] Divo E, Kassab AJ. An efficient localized radial basis function meshless method for fluid flow and conjugate heat transfer. J Heat Transf 2006;129(2):124–36. http://dx.doi.org/10.1115/1.2402181.
[23] Roy C. Strategies for driving mesh adaptation in CFD. In: 47th AIAA aerospace sciences meeting including the new horizons forum and aerospace exposition. 2009, p. 1302. http://dx.doi.org/10.2514/6.2009-1302.
[24] Zamolo R, Bacer L, Miotti D, Nobile E, Munerato M. RBF-FD meshless simulation of 3D fully developed flow and heat transfer in triply periodic minimal surfaces. Int J Heat Mass Transfer 2025;242:126798. http://dx.doi.org/10.1016/j.ijheatmasstransfer.2025.126798.
[25] Zongmin W. Hermite-Birkhoff interpolation of scattered data by radial basis functions. Approx Theor Appl 1992;8:1–10. http://dx.doi.org/10.1007/BF02836101.
[26] Narcowich FJ, Ward JD. Generalized Hermite interpolation via matrix-valued conditionally positive definite functions. Math Comp 1994;63(208):661–87. http://dx.doi.org/10.2307/2153288.
[27] Sun X. Scattered Hermite interpolation using radial basis functions. Linear Algebra Appl 1994;207:135–46. http://dx.doi.org/10.1016/0024-3795(94)90007-8.
[28] Hardy RL. Multiquadric equations of topography and other irregular surfaces. J Geophys Res 1971;76(8):1905–15. http://dx.doi.org/10.1029/JB076i008p01905.
[29] Šarler B. A radial basis function collocation approach in computational fluid dynamics. CMES - Comp Model Eng 2005;7(2):185–94. http://dx.doi.org/10.3970/cmes.2005.007.185.
[30] Zamolo R, Parussini L. Analysis of geometric uncertainties in CFD problems solved by RBF-FD meshless method. J Comput Phys 2020;421:109730. http://dx.doi.org/10.1016/j.jcp.2020.109730.
[31] Flyer N, Fornberg B, Bayona V, Barnett G. On the role of polynomials in RBF-FD approximations: I. interpolation and accuracy. J Comput Phys 2016;321:21–38. http://dx.doi.org/10.1016/j.jcp.2016.05.026.
[32] Bayona V, Flyer N, Fornberg B, Barnett GA. On the role of polynomials in RBF-FD approximations: II. Numerical solution of elliptic PDEs. J Comput Phys 2017;332:257–73. http://dx.doi.org/10.1016/j.jcp.2016.12.008.
[33] Bayona V, Flyer N, Fornberg B. On the role of polynomials in RBF-FD approximations: III. Behavior near domain boundaries. J Comput Phys 2019;380:378–99. http://dx.doi.org/10.1016/j.jcp.2018.12.013.
[34] Kolar-Požun A, Jančič M, Rot M, Kosec G. Some observations regarding the RBF-FD approximation accuracy dependence on stencil size. J Comput Sci- Neth 2024;79:102284. http://dx.doi.org/10.1016/j.jocs.2024.102284.
[35] Fasshauer GE. Meshfree Approximation Methods with Matlab. WORLD SCIENTIFIC; 2007, http://dx.doi.org/10.1142/6437.
[36] Stevens D, Power H, Meng C, Howard D, Cliffe K. An alternative local collocation strategy for high-convergence meshless PDE solutions, using radial basis functions. J Comput Phys 2013;254:52–75. http://dx.doi.org/10.1016/j.jcp.2013.07.026.
[37] Jančič M, Kosec G. Stability analysis of RBF-FD and WLS based local strong form meshless methods on scattered nodes. In: 2022 45th jubilee international convention on information, communication and electronic technology. MIPRO, 2022, p. 275–80. http://dx.doi.org/10.23919/MIPRO55190.2022.9803334.
[38] Tominec I, Nazarov M, Larsson E. Stability estimates for radial basis function methods applied to linear scalar conservation laws. Appl Math Comput 2025;485:129020. http://dx.doi.org/10.1016/j.amc.2024.129020.
[39] Chorin AJ. A numerical method for solving incompressible viscous flow problems. J Comput Phys 1967;2(1):12–26. http://dx.doi.org/10.1016/0021-9991(67)90037-X.
[40] Zamolo R, Nobile E. Solution of incompressible fluid flow problems with heat transfer by means of an efficient RBF-FD meshless approach. Numer Heat Tr B-Fund 2019;75(1):19–42. http://dx.doi.org/10.1080/10407790.2019.1580048.
[41] Shepard D. A two-dimensional interpolation function for irregularly-spaced data. In: Proceedings of the 1968 23rd ACM national conference. 1968, p. 517–24. http://dx.doi.org/10.1145/800186.810616.